Aeroelasticity of Nonlinear Tail / Rudder Systems with Freeplay

Evan Rishel

A thesis
submitted in partial fulfillment of the
requirements for the degree of

Master of Science in Aeronautics and Astronautics

University of Washington

2015

Reading Committee:
Eli Livne, Chair
Keith Holsapple

Program Authorized to Offer Degree:
Aeronautics & Astronautics

University of Washington

Abstract

Aeroelasticity of Nonlinear Tail / Rudder Systems with Freeplay

Evan Rishel

Chair of the Supervisory Committee:
Professor Eli Livne
Aeronautics and Astronautics

This thesis details the development of a linear/nonlinear three degree of freedom aeroelastic system designed and manufactured at the University of Washington (UW). Describing function analysis was carried out in the frequency domain. Time domain simulations were carried out to account for all types of motion. Nonlinear aeroelastic behavior may lead to limit cycles which can be captured in the frequency domain using describing function approximation and numerically using Runga-Kutta integration. Linear and nonlinear aeroelastic tests were conducted in the UW 3x3 low-speed wind tunnel to determine the linear flutter speed and frequency of the system as well as its nonlinear behavior when freeplay is introduced. The test data is presented along with the results of the MATLAB-based simulations. The correlation between test and numerical results is very high.

TABLE OF CONTENTS

LIST OF FIGURES

LIST OF TABLES

ACKNOWLEDGMENTS

First and foremost I would like to thank my advisor, Professor Eli Livne who spent countless hours teaching, mentoring and developing my technical understanding of the field of aeroelasticity. His outstanding dedication made this a very fulfilling and enjoyable experience.

I'd also like to that those who aided me with the testing and development of the UW system. First I'd like to thank Research Engineer, Bill Kuykendall, who spent many hours aiding me in the construction of system modifications. I learned many valuable practical engineering skills through him and for that I am very grateful. I would also like to thank Research Engineer, Fiona Spencer, who went out of her way to accommodate my needs in conducting the wind tunnel tests.

Finally I'd like to thank my family, whose constant support, guidance and love has molded me into the man I am now. A man that always seeks to learn, improve and take full advantage of the gifts that God has given him.

DEDICATION

I dedicate this thesis to my parents, Andy and Sherry. May my works be continually pleasing to you and Him.

NOMENCLATURE

Acronyms

d.o.f.	Degree of freedom
LCO	Limit cycle oscillations
LTI	Linear time invariant
SMH	Simple harmonic motion

Symbols

T_i	i^{th} Theodorsen constant (ref Appendix B)
L	Aerodynamic lift
M_α, M_β	Aerodynamic moment of tail-rudder and of rudder
x_β	Center of gravity of the rudder from c, normalized by b
x_α	Center of gravity of the tail/rudder from a, normalized by b
U	Free stream velocity
Q_{q_i}	Generalized forces of Lagrangian dynamics
Q_D	Generalized structural damping forces
I_α, I_β	Moments of inertia of tail-rudder about a and of rudder about c
P	Negative of aerodynamic lift $P = -L$
c	Non-dimensional distance from airfoil mid-chord to control surface (rudder) hinge line, w.r.t the semi-chord
a	Non-dimensional distance from airfoil mid-chord to elastic axis, w.r.t the semi-chord
h	Plunge displacement
k	Reduced frequency, $\frac{kb}{U}$

$\mathbf{P_i}$	Roger approximation matrices
b	Semi-chord
S_α, S_β	Static moments of tail-rudder about a and of rudder about c
K_h	Stiffness of tail in deflection
g	Structural damping coefficient
G_{st}	Structural damping matrix
$K_{\beta,eq}$	Structural damping matrix
$C(k)$	Theodorsen circulation coefficient
$3D$	Three dimensional
K_α, K_β	Torsional stiffness of tail about a and of rudder about c
M	Total mass of tail-rudder and support blocks
$2D$	Two dimensional
C	Viscous damping matrix

Greek Symbols

β_n	Aerodynamic lag roots (Roger Approximation)
δ	Angular size of the freeplay region
ζ	Damping ratio
λ	Eigenvalue
ρ	Freestream air density
α	Pitch angle about the elastic axis
η	Ratio of orifice to piston areas $\frac{A_{orf}}{A_p}$
β	Rudder (flap) angle about the hinge line
ω	Uncoupled natural frequency

Chapter 1
INTRODUCTION

1.1 Background

The field of aeroelasticity is an integration of a number of engineering disciplines which cover the interaction between elastic, inertial and aerodynamic loads on flexible aerospace structures. This interaction can be visualized in the block diagram below, which illustrates the feedback loop of an aeroelastic system. This feedback loop is often referred to as the aeroelastic plant.

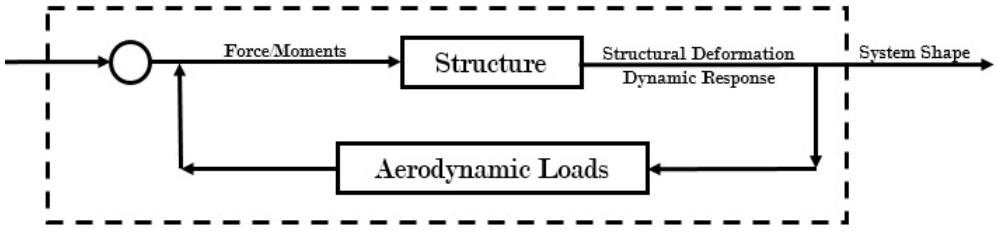

Figure 1.1: Feedback loop representing the aeroelastic plant.

Aeroelastic systems, like conventional aircraft, have the propensity to extract large amounts of energy from the airstream. As such, the aeroelastic behavior of such systems receives considerable attention in the design process to ensure catastrophic failure of the structure is avoided. Aeroelastic behavior can most often be adequately predicted and analyzed via computer-based simulations in conjunction with wind tunnel experimentation. The intent of this research is to use such techniques to analyze the effects of nonlinearities on the behavior of a three degree of freedom (d.o.f.) aeroelastic system and in doing so advance the simulation tools and experimental ca-

pabilities of the University of Washington in the aeroelasticity area. The nonlinearity considered here is control surface freeplay, a zero stiffness region that can develop from loose or fatigued hardware or mechanical linkages.

The system studied in this research is based on a system of similar design used by Duke University [1][2][3]. This system, referred to as a typical aeroelastic section, is composed of a wing section with a trailing-edge control surface. The section is mounted with plunge, pitch and control surface springs as detailed in Figure 1.2 as to simulate the stiffness and damping seen by a conventional, flexible tail/rudder system.

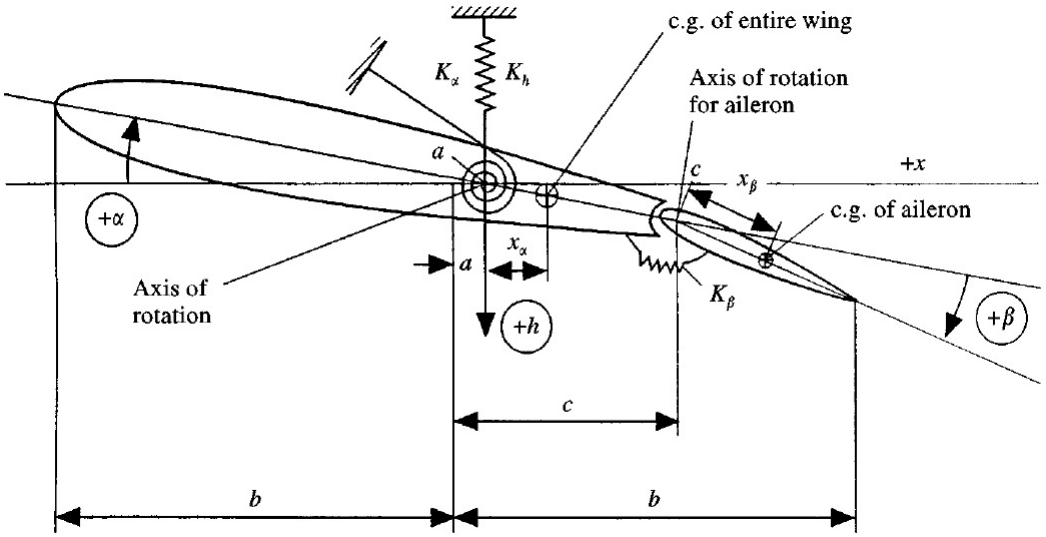

Figure 1.2: Schematic of typical 3 d.o.f. aeroelastic section with control surface[2].

1.1.1 Nonlinear Aeroelasticity

Nonlinear aeroelastic behavior, including limit-cycle oscillation (LCO), has been studied theoretically by several research groups. At Duke University, lead by *Conner, et al.* [1][2][3] numerical studies on control surface freeplay were conducted by modeling it theoretically as a system of piecewise linear state-space models which can be numerically integrated. This piecewise torque/rotation behavior of the trailing edge flap can be visualized in Figure 1.3. Here δ is defined as the size of half

the freeplay region. The experimental model previously described was used to validate this theoretical model. In both cases limit-cycle oscillations were discovered to occur at velocities considerably lower than the linear flutter speed of the system, a phenomenon which can have detrimental effects on the performance and structural integrity of an aircraft.

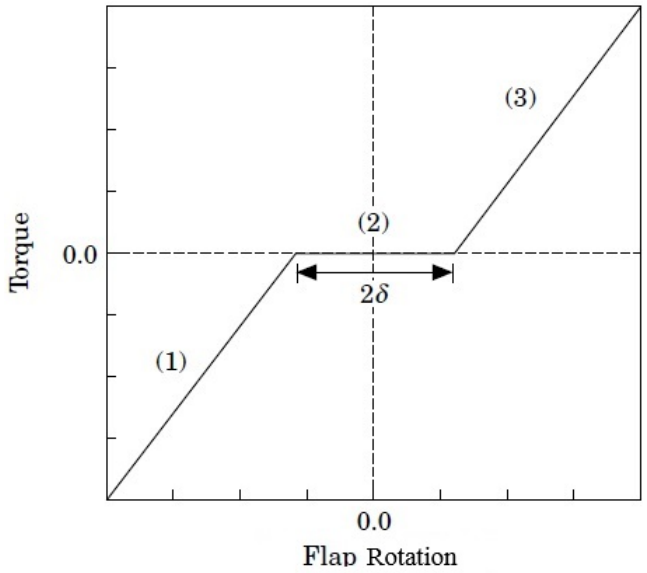

Figure 1.3: Piecewise restoring moment due to K_β with a symmetric freeplay region [2][3].

In Refs [4][5] nonlinear stability analyses of control surface flutter of a typical 3 d.o.f. aeroelastic section with freeplay were reported. An analytic describing function method was used to predict LCO amplitudes, and a continuation method used to track the flutter modes. The describing function technique utilizes frequency domain unsteady aerodynamics to simulate aeroelastic behavior, the details of which will be discussed later. The results compared well to direct integration of the equations of motion using rational function approximation of time domain aerodynamics as well as experimental data [5].

Both frequency domain describing function and time domain direct integration

simulations are used in the research presented in this paper due to their distinct advantages. Describing function simulations provide a computationally efficient means of predicting limit-cycle behavior while offering the capability of predicting the presence of multiple limit-cycles and assessing their stability. One limitation of the describing function method is that it is limited to simple harmonic motion (SHM). Direct time integration, however, is capable of predicting motions in addition to those that are simple harmonic, namely convergent, divergent and non-periodic. Thus in order to completely characterize and analyze the system, both computation methods should be used.

Limit-Cycle Oscillation (LCO)

In nonlinear systems, especially those with nonlinear stiffening terms, the amplitude of oscillations from a disturbance can grow until a limit-cycle oscillation is reached. A limit-cycle is an isolated, closed trajectory in phase space. Neighboring trajectories, however, are not closed and may either spiral towards or away from the limit cycle based on its stability - a subject addressed in later sections. It is important to note that LCOs are inherently nonlinear phenomenon and do not occur in linear systems. LCOs are not necessarily a result of an instability but can be induced by large disturbances in the case of a stable equilibrium state. That is to say, given a sufficiently large initial condition, the system can respond by falling into a limit-cycle where the amplitude is dependent on the initial condition. LCOs are very difficult to predict due to their nonlinear nature and reliable approximation techniques are still being sought. Stable LCOs, which exhibit self-sustained oscillation, are of interest to aerospace engineers in the case of flexible wings because of their propensity for causing structural fatigue. Considerable attention will thus be focused on the subject throughout this research [6].

1.2 Objectives

This research seeks to analyze the linear flutter properties of and the effects of nonlinear freeplay on the behavior of the UW 3 d.o.f. 2D tail/rudder experimental system.

Specifically, the goals of this research are to:

- Accurately characterize the system properties to include structural properties and modal frequencies.
- Develop numerical simulations for the 3 d.o.f. aeroelastic section in a 2-D unsteady, incompressible flow-field[7] capable of incorporating a freeplay nonlinearity [8].
- Conduct linear flutter tests with rudder freeplay in which linear flutter characteristics are compared to those predicted analytically.
- Conduct nonlinear tests in which limit cycles are obtained and compared to those predicted by describing function and numerical integration simulations.
- Consider areas of uncertainty and determine means of minimizing sources of error in math modeling techniques.

1.3 Thesis Structure

The thesis begins with a presentation of the aeroelastic equations of motion for a 3 d.o.f. linear system in Chapter 2.

Complete characterization of the experimental model to include structural properties, data measurement, and acquisition equipment and structural dynamics is done in Chapter 3.

The linear flutter of the UW system is considered in Chapter 4. It takes the reader through the analytical derivation of the linear flutter problem in both the frequency and time domains. It also details linear flutter tests in the UW low speed 3x3 wind tunnel and compares the results of both.

Chapter 5 explains the incorporation of the freeplay nonlinearity and the derivation of the describing function approximation. How the results are interpreted and limit cycle stability in this domain are also considered.

Chapter 6 considers the time domain method of incorporating freeplay into the mathematical model. Results generated via numerical integration are compared to those produced in the frequency domain in the previous chapter.

Finally, the experimental tests of the nonlinear system with freeplay and their results are considered in Chapter 7. These results are compare to both simulations and their accuracy is evaluated.

The thesis ends with concluding remarks and proposed areas of future research.

Chapter 2

EQUATIONS OF MOTION OF THE AEROELASTIC SYSTEM

Because the numerical simulations and aeroelastic tools presented in this research are founded on a unique set of equations of motion, it is necessary that a thorough understanding of the origins of these equations be established before proceeding. The equations of motion of the aeroelastic system describe the behavior of the system and are derived using Legrangian mechanics in combination with Theodorsen's unsteady aerodynamic approximations [7].

The benefit of the Legrangian approach in complex, dynamic systems is that the equations of motion hold true for any coordinate system through the use of energy entities and generalized coordinates. The generalized coordinates selected for the three d.o.f. aeroelastic system are h, α and β, the plunge, pitch and rudder degrees of freedom, respectively defined in Figure 1.2. Here, h is defined to be positive for pure plunging motion downward. Its origin is located at the shear center, or elastic axis, of the airfoil at a non-dimensional distance a from the half-chord. The pitch d.o.f. α is defined to be positive for clockwise rotation. The rudder d.o.f. β is about the control surface hinge line and defined to be positive for clockwise rotation.

2.1 Structural Contributions

2.1.1 Kinetic and Potential Energy

Derived from Newton's laws, the Legrangian formulation for a multiple d.o.f. system can be written in the following form, where L is known as the Legrangian and is equal to the total kinetic energy minus the total potential energy, i.e. $L = T - U$.

Generalized forces corresponding to the action of non-conservative forces are denoted Q_i

$$\frac{d}{dt}\left(\frac{\partial L}{\partial q_i}\right) - \frac{\partial L}{\partial q_i} = Q_i \tag{2.1}$$

The total kinetic energy of the aeroelastic system is equal to the sum of the kinetic energies of each component. The kinetic energy of the wing section is determined by integrating the contributions along the section from $x = 0$ to $x = b + c$ and defined in Figure 1.2. The same can be said for the rudder contribution which is integrated from $x = b + c$ to $x = 2b$ [8]. The sum can be written in matrix form as follows:

$$T = \frac{1}{2}\begin{Bmatrix} \dot{h} & \dot{\alpha} & \dot{\beta} \end{Bmatrix} \begin{bmatrix} M & S_\alpha & S_\beta \\ & I_\alpha & (I_\beta + b\,(c-a)\,S_\beta) \\ sym & & I_\beta \end{bmatrix} \begin{Bmatrix} \dot{h} \\ \dot{\alpha} \\ \dot{\beta} \end{Bmatrix} \tag{2.2}$$

The definitions of the entries of the above equation can be found in nomenclature section.

The potential energy of the system is composed of the strain energy and gravitational potential energy of the system, however, given the vertical positioning of the tail, the gravitational contribution is assumed to be negligible. The strain energy of the system is composed of the total work done in deforming the springs in each d.o.f. Assuming no deformation at $h = \alpha = \beta = 0$ the total strain energy in the system can be written in the following matrix form:

$$U = \frac{1}{2}\begin{Bmatrix} h & \alpha & \beta \end{Bmatrix} \begin{bmatrix} K_h & 0 & 0 \\ 0 & K_\alpha & 0 \\ 0 & 0 & K_\beta \end{bmatrix} \begin{Bmatrix} h \\ \alpha \\ \beta \end{Bmatrix} \tag{2.3}$$

Here K is used as the symbol for stiffness coefficient rather than C used in Figure 1.2 to avoid confusion with the symbol for viscous damping used later. In-

serting the equations for kinetic and potential energy into Eq. 2.1 and noting that $\frac{\partial T}{\partial q_i} = \frac{\partial U}{\partial \dot{q}_i} = 0$, the equation for an undamped, unforced 3 d.o.f. system is attained. This equation can be written in condensed notation as follows:

$$\mathbf{M_s}\ddot{\mathbf{q}} + \mathbf{K_s}\mathbf{q} = \mathbf{0} \tag{2.4}$$

where $\mathbf{M_s}$ and $\mathbf{K_s}$ represent the mass and stiffness matrices defined above and $\mathbf{q}$ represents the matrix of generalized coordinates $\begin{Bmatrix} h & \alpha & \beta \end{Bmatrix}^T$. The addition of damping and generalized forcing to this equation will now be considered.

2.1.2 Structural Damping

Viscous Damping

In typical dynamic systems energy dissipated is in the form of damping. In viscous damping, damping forces are linearly dependent on rates of change of generalized displacements. Generalized forces due to viscous damping are:

$$\{\mathbf{Q}\} = [\mathbf{C}]\{\dot{\mathbf{q}}\} \tag{2.5}$$

where:

$$\mathbf{C} = \begin{bmatrix} 2m_{hh}\zeta_h\omega_h & 0 & 0 \\ 0 & 2m_{\alpha\alpha}\zeta_\alpha\omega_\alpha & 0 \\ 0 & 0 & 2m_{\beta\beta}\zeta_\beta\omega_\beta \end{bmatrix} \tag{2.6}$$

and where ζ_i is the measured damping ratio, ω_i is the uncoupled natural frequency and m_{ii} is the structural mass of each d.o.f.

Hysteretic Damping

The hysteretic damping model available for simple harmonic motions only assumes that energy is dissipated in proportion to the amplitude of oscillation, or stiffness, but in phase with velocity. For SHM, using complex notion, the displacement and velocity of each degree of freedom can be written as $q(t) = q_0 e^{j\omega t}$ and $\dot{q}(t) = j\omega q_0 e^{j\omega t}$. The restoring force from a hysteretic damping model in a single d.o.f., proportional to elastic force and in phase with velocity is thus $F_0 = jgKq$. Here g refers to the structural damping coefficient of the d.o.f. in question. For lightly damped single d.o.f. systems, excitation over a spectrum of frequencies yields an oscillatory response at the resonance frequency. Consequently, for such systems the equality $g = 2\zeta$ can be assumed to relate viscous and structural damping. With this relation the hysteretic damping model can be defined for simple harmonic motions:

$$\{\mathbf{Q}\} = j\,[\mathbf{H}]\,\{\mathbf{q}\} \tag{2.7}$$

where:

$$\mathbf{H} = j \begin{bmatrix} g_h K_h & 0 & 0 \\ 0 & g_\alpha K_\alpha & 0 \\ 0 & 0 & g_\beta K_\beta \end{bmatrix} \tag{2.8}$$

This can be written compactly as $j\mathbf{G_{st}K_s}$ where $\mathbf{K_s}$ is the stiffness matrix defined above and $\mathbf{G_{st}}$ is the structural damping matrix.

2.2 Generalized Forces

Generalized forces are founded on the concept of virtual work. For an aeroelastic system these forces include nonconservative damping forces and aerodynamic forces. Generalized force for the single d.o.f. system studies here can be conceptualized as the virtual work done when the system changes motion by $\delta h, \delta\alpha$, or $\delta\beta$. In equation form:

$$Q_{q_i} = \frac{\partial \delta W}{\partial \delta q_i} \tag{2.9}$$

For a viscous damping model, the generalized forces due to nonconservative damping can be summarized in the following matrix form.

$$\begin{Bmatrix} Q_h \\ Q_\alpha \\ Q_\beta \end{Bmatrix} = - \begin{bmatrix} c_h & 0 & 0 \\ 0 & c_\alpha & 0 \\ 0 & 0 & c_\beta \end{bmatrix} \begin{Bmatrix} \dot{h} \\ \dot{\alpha} \\ \dot{\beta} \end{Bmatrix} \tag{2.10}$$

The aerodynamic contribution to the generalized force expression accounts for the externally applied forces and moments due to airflow over the model. These forces are the lifting force, P, (in the down direction), the pitching moment about the elastic axis, M_α, and the moment of the control surface about its hinge line, H_β. As before, the virtual work done by the forces and moments in response to perturbed motion in the three degrees of freedom constitutes the generalized force. Adding this contribution to the damping terms:

$$\begin{Bmatrix} Q_h \\ Q_\alpha \\ Q_\beta \end{Bmatrix} = - \begin{bmatrix} c_h & 0 & 0 \\ 0 & c_\alpha & 0 \\ 0 & 0 & c_\beta \end{bmatrix} \begin{Bmatrix} \dot{h} \\ \dot{\alpha} \\ \dot{\beta} \end{Bmatrix} + \begin{Bmatrix} P \\ M_\alpha \\ H_\beta \end{Bmatrix} \tag{2.11}$$

The means of determining the aerodynamics terms used in this research is known as the Theodorsen method.

2.2.1 Aerodynamic Contribution

The Theodorsen method is based on potential flow theory and the Kutta condition. Flow expressions resulting in incompressible forces and moments on an airfoil with unsteady motion are composed of non-circulatory and circulatory components. Using complex variable theory and conformal transformations, flow around an airfoil can be represented by a superposition of the solutions to the potential flow equation $\nabla^2\phi = 0$. Motion of the system is represented via source/sink solution pairs located along the surface of the airfoil. These non-circulatory pairs are placed in such a way that at the point of their location velocity is purely vertical and parallel to the surface everywhere else. Flow velocity is calculated via the integration of each doublet over the surface of the airfoil. This integration, however, yields a infinite velocity singularity at the trailing edge which must be eliminated to satisfy the Kutta condition.

The Kutta condition is satisfied by the introduction of wake vortices. Because the wake is a series of vortices formed by sinusoidal motion in time, it may be considered as a sinusoidal variation of vortex distribution in space. As such, vortices are placed along the wake starting from the trailing edge while placement of counter-vortices on the airfoil surface ensures that circulation is preserved. Addition of the contributions of the wake vortices to the source/sink doublets at the trailing edge imposes the Kutta condition [7][9].

The problem thus resolves itself into a combination of definite integrals which lead to the Theodorsen Function involving Bessel functions of the first and second kind.

$$C(k) = \frac{\int_1^\infty \frac{x_0}{\sqrt{x_0^2-1}} e^{-ikx_0} dx_0}{\int_1^\infty \frac{\sqrt{x_0+1}}{\sqrt{x_0-1}} e^{-ikx_0} dx_0} = F(k) + iG(k) \tag{2.12}$$

Here, the functions are written in terms of the reduced frequency of oscillation, $k = \frac{\omega b}{U}$. The parameter k is used because the unsteadiness of the flow is relative to the airfoil length and wake wavelength. From these functions the net pressure

difference over the surface, $p(x)$ can be determined. The total forces and moments follow via the integration of the pressure distribution over the surface. Theodorsen derived these through the introduction of his T-functions which are a function of the geometry of the system. These T-functions as well as the subsequent expressions for the total forces and moments can be found in Appendix A. For a detailed derivation and explanation the reader is directed to Refs[7] or [9].

Because Theodorsen's method is restricted to SHM the total aerodynamic forces and moments can be expressed as an aerodynamic matrix and a vector of states multiplied by the dynamic pressure. The aerodynamic matrix is complex and a function of the reduced frequency of the system.

$$\begin{Bmatrix} P \\ M_\alpha \\ H_\beta \end{Bmatrix} = \frac{1}{2}\rho_\infty U_\infty^2 \left[A(jk)\right] \begin{Bmatrix} h \\ \alpha \\ \beta \end{Bmatrix} \tag{2.13}$$

This final component can be added to the generalized forces due to non-conservative damping to fully define the equations of motion of the aeroelastic system.

$$\mathbf{M_s}\ddot{\mathbf{q}} + \{\mathbf{Q_D}\} + \mathbf{K_s q} = \frac{1}{2}\rho_\infty U_\infty^2 \mathbf{A(jk)q} \tag{2.14}$$

The addition of the structural viscous term $\mathbf{Q_D} = \mathbf{C}\dot{\mathbf{q}}$ or the hysteretic term $\mathbf{Q_D} = j\mathbf{G_{st}K_s q}$ can be made based on the damping model desired. This will vary based on the solution method used.

Chapter 3
EXPERIMENTAL AEROELASTIC SYSTEM

The 3 d.o.f aeroelastic system built at the University of Washington and used for flutter and LCO testing in the University's 3'x3' low speed wind tunnel replicates the design used by the research group at Duke University [1][2][3]. The design accurately simulates the typical aeroelastic section illustrated in Figure 1.2. This chapter details the design, construction, and characterization of this system.

3.1 Model Design

The University of Washington experimental aeroelastic model was designed and manufactured in the Mechanical Engineering Machine Shop by William F. Kuykendall, Lab Engineer, ME, and Freancesca Paltera, MSME Student, and consists of an aluminum-composite tail/rudder system mounted vertically on a series of leaf springs as seen in the following figures [10]. The wing construction is based on a 2-D design composed of a symmetric NACA 0012 two section airfoil. The first section is the main body of the wing, which has a 0.381 m chord and 0.9017 m span and is a spar-rib construction with the main spar located at the section's quarter chord. The second section is the 0.127 m chord, 0.9017 m span rudder section constructed from carbon fiber reinforced plastic (CFRP). The rudder section is connected to the trailing edge of the main body along a hinge line via two aluminum hinge pins. The following figures detail the design of the aeroelastic system.

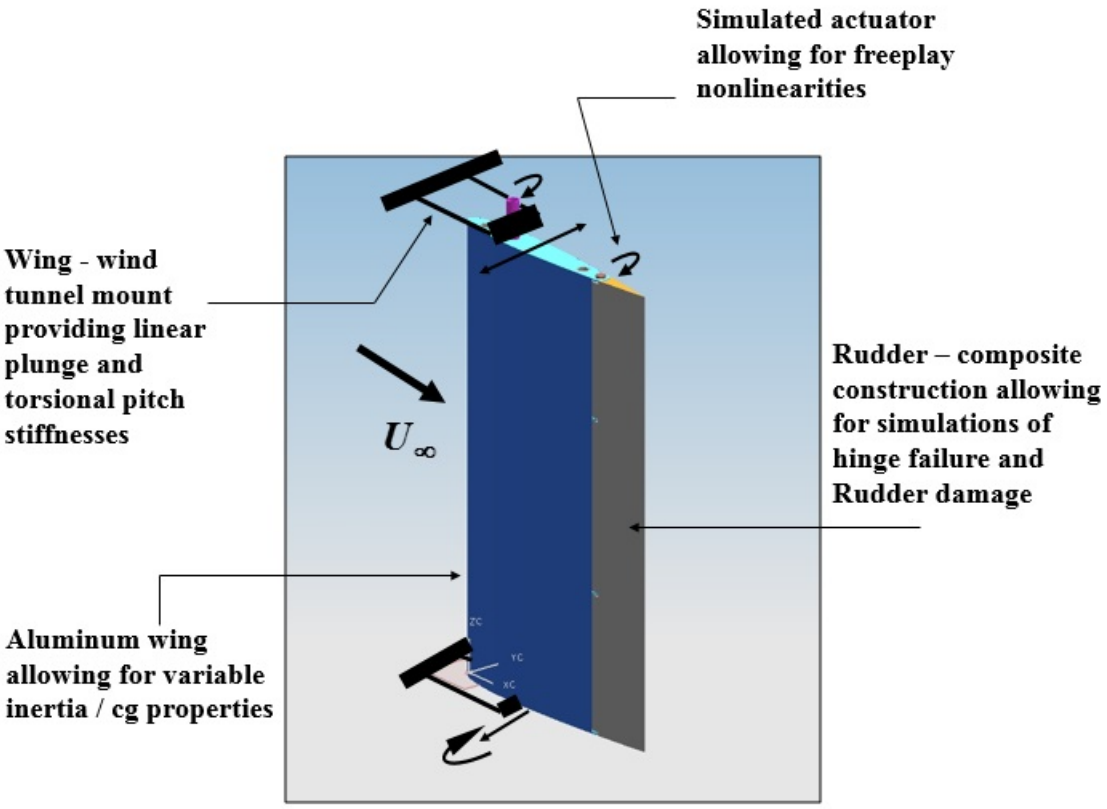

Figure 3.1: Annotated CAD model of experimental aeroelastic

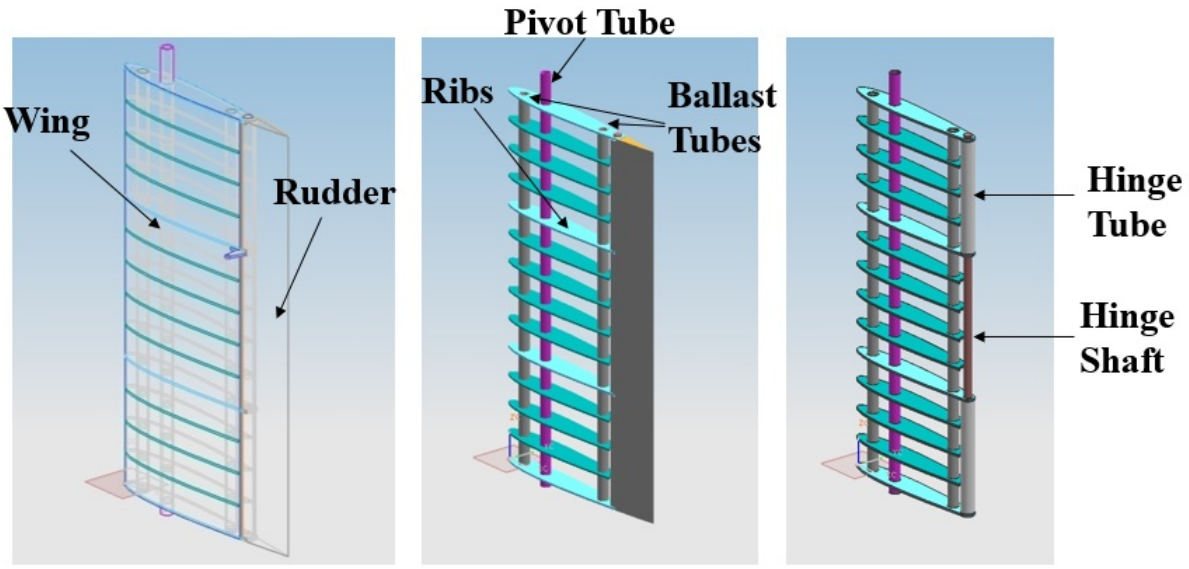

Figure 3.2: CAD model of tail/rudder construction

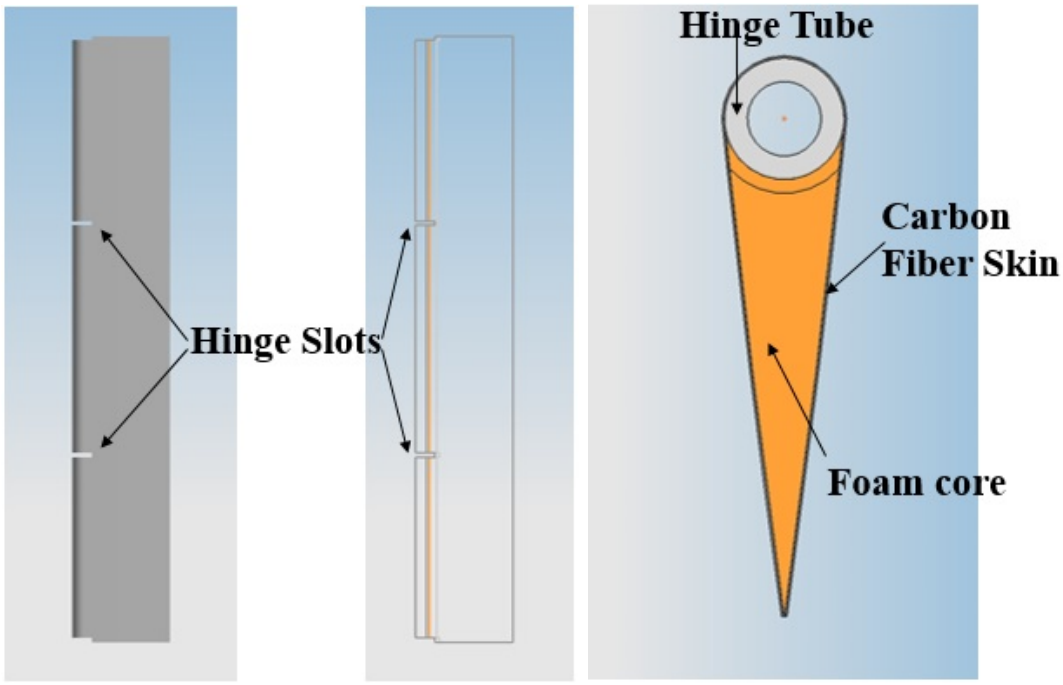

(a) Front view of rudder construction with hinge slots *(b)* Top view of rudder construction

Figure 3.3: CAD model views of rudder construction

The entire system is held by aluminum support blocks via the main spar, which rests in the blocks on thrust bearings permitting pitch rotation. Restoring forces in each d.o.f. are achieved via three custom spring designs all of which are shown in Figure 3.5. The plunge d.o.f. uses four 29.85 x 7.62 x 0.158 *cm* steel leaf springs acting as bi-cantilever beams. Pitch stiffness is achieved via eighth inch steel rods fitted through a collar attached to the main spar of the system. These rods are fed through a set of L-brackets mounted, along with the leaf springs, to the set of aluminum support blocks. Rudder stiffness is generated via a single eighth inch steel rod attached to the rudder hinge line and restrained by a series of screws. These screws can be adjusted as illustrated in Figure 3.5 to introduce freeplay into the system.

Figure 3.4: University of Washington aeroelastic system mounted in lab [8].

The system has the capability of adding a second nonlinearity in the form of dampers that provide velocity squared damping to the rudder d.o.f. as seen in Figure 3.4. The dampers and their nonlinearity are not considered in this paper.

3.2 Measurement Sensors

All data is collected and managed via a Jaguar Spectral Dynamics data acquisition system operating on a SUSE Linus (10.0) platform. Data recorded can be displayed

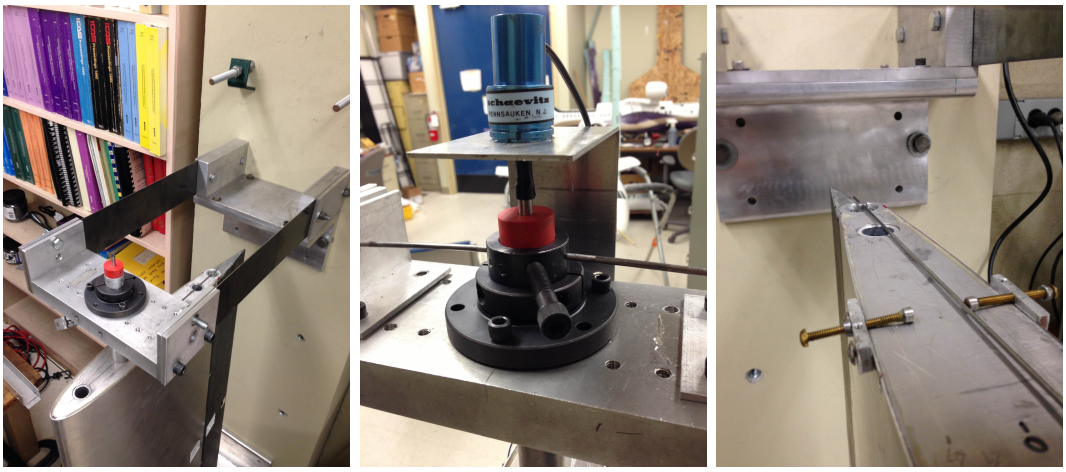

(a) Upper leaf springs and support blocks

(b) Pitch d.o.f. springs and RVDT sensor

(c) Rudder d.o.f. leaf spring and freeplay support screws

Figure 3.5: Experimental model springs and freeplay support mechanism

graphically, manipulated via Fourier Transforms, and exported to a numerical computing environment such as MATLAB.

The plunge degree of freedom motion is measured using a Polytec OFV-5000 Laser Vibrometer capable of recording instantaneous velocities and displacements. The sensitivities, which are variable via the vibrometer controller were selected as 1000 $\frac{mV}{\frac{m}{sec}}$ and 200 $\frac{mV}{mm}$ respectively. The velocity and displacement ranges of the vibrometer are 1.25 $\frac{m}{sec}$ and 200 mm. The pitch and rudder rotational degrees of freedom are measured via rotational variable displacement transducers (RDVT). The pitch RDVT is mounted on top of the pitch axis and seen in Figure 3.5 and has a sensitivity of 125 $\frac{mV}{degree}$ and a range of 56.56°. The rudder RVDT is mounted at the base of the wing section inside the main tail section and has a sensitivity of 29 $\frac{mV}{degree}$ and range of 121.91°.

3.3 Structural Properties

Characterization of the structural properties was conducted with the wing system mounted in the lab as shown in Figure 3.4. The properties of interest for fully characterizing the behavior of the system are component and collective masses, stiffness and damping coefficients and single d.o.f. and coupled natural frequencies.

Each component was weighed to determine individual mass contributions. Stiffnesses were determined by systematically reducing the system to one degree of freedom by mechanically constraining all but one d.o.f. Each d.o.f. is then displaced with a force gauge and the displacements are measured with the Jaguar system as well as an analog dial gauge. Inertial properties were output by CAD component models and validated by manipulating the equations of motion. Inertial properties can be varied via ballast weight through hollow spars in the wing's construction to tailor the system's linear flutter speed. Damping coefficients were measured in a similar way to the stiffnesses by perturbing each uncoupled, single d.o.f. by an initial displacement and recording the time history with the Jaguar system. The logarithmic decrement and half-power methods were used to determine the overall coefficient values.

The logarithmic decrement method is a time domain tool that utilizes the natural log of the ratio of adjacent peak amplitudes, δ, to calculate the damping ratio, ζ, of an under-damped system in free decay vibration as shown below. The variable n represents the number of cycles being averaged.

$$\delta = \frac{1}{n} ln \frac{x(t)}{x(t+nT)}, \qquad \zeta = \frac{1}{\sqrt{1+(\frac{2\pi}{\delta})^2}}$$

3.3.1 Nonlinear Damping and Nominal Damping Values

When determining the log decrement damping ratios, subtle nonlinearities emerged in the α and β degrees of freedom. These nonlinearities create a dependence of damping ratio on initial displacement of the d.o.f. and the number of peaks averaged in

determining the log decrement value. The trends showed a subtle increase in damping ratio with initial displacement and a notable increase in ratio with the number of peaks averaged from the first peak of initial disturbance. This nonlinearity introduces an element of uncertainty that must be considered in the simulations. The nonlinearities in pitch and rudder damping will not be fully characterized in this research but will be accounted for in an uncertainty analysis in subsequent sections. As such, ratios averaged over a span of initial displacement angles and a reasonable number of cycles will be used as nominal damping values. These values will be used to generate

Table 3.1: Nominal System Parameters of the Experimental Model

Geometry	
Half-chord, b	0.26 m
Span	0.915 m
Elastic axis, a w.r.t. b	-0.454
Hinge line, c, w.r.t. b	0.527
Mass	
Mass of wing section	6.468 kg
Mass of rudder	0.436 kg
Mass of support blocks	4.301 kg
Mass of pitch RVDT sensor	0.136 kg
Mass of pitch springs	0.226 kg
Mass of leaf springs	1.509 kg
Inertia	
S_α	0.37309 $kg-m$
S_β	0.02223 $kg-m$
x_α	0.054
x_β	0.051
I_α	0.1362 $kg-m^2$
I_β	0.0015 $kg-m^2$
Stiffness	
K_h	4646 $\frac{N}{m}$
K_α	100.4 $\frac{N-m}{rad}$
K_β	3.9 $\frac{N-m}{rad}$
Damping	
ζ_h	0.005
ζ_α	0.019
ζ_β	0.058

baseline simulations and can be found in Table 3.1 along with a complete list of the structural properties for the UW experimental system.

3.4 System Structural Dynamics: Modal Testing and System Natural Frequencies

A series of modal tests conducted on the system using the laser vibrometer and the Jaguar data acquisition system yielded the single d.o.f. and couple natural frequencies of the system. Single d.o.f. tests were conducted by constraining all but one d.o.f., exciting the structure with an impact hammer and collecting the velocity data with the vibrometer. Using the Jaguar's built-in transfer function capability, the frequency response is visualized as a spike corresponding to the natural frequency of the respective d.o.f. The coupled frequencies of the system were similarly determined by impacting the unconstrained structure and analyzing the modal response. The response of the couple system displays three peaks, each corresponding to its respective d.o.f. The modal test results are summarized below in Table 3.2

Table 3.2: Natural Frequencies of the Experimental Model

	Fully Coupled		
	Analytical	Measured	% Difference
ω_h	2.89 Hz	2.73 Hz	5.86%
ω_α	4.47 Hz	4.49 Hz	0.44%
ω_β	9.79Hz	9.06 Hz	8.1%

3.4.1 Analytical Frequencies and System System Fine-Tuning

When constrained to a single degree of freedom, the system of equations reduces to a single uncoupled equation, where m_{qq}, c_q and k_q refer to the diagonal terms corresponding the d.o.f. in question q. This equation can be manipulated to derive the expression for single d.o.f. natural frequency.

$$m_{qq}\ddot{q} + c_q\dot{q} + k_q q = \frac{1}{2}\rho_\infty U_\infty^2 A(jk)q \quad \Longrightarrow \quad \omega_q = \sqrt{\frac{k_q}{m_{qq}}}$$

The coupled natural frequencies can be analytically evaluated by solving the eigenvalue problem detailed in the next chapter. The frequencies determined for the UW system are summarized in Table 3.2. Initial discrepancies between predicted and measured values suggested that some mass and inertial effects were not captured by the model. Fine-tuning of the diagonal mass terms using the ratio of predicted to measured single d.o.f. frequency values yielded better agreement between the coupled frequencies and was thus implemented.

3.5 Wind Tunnel

The model is designed to be mounted vertically in the University of Washington 3x3 low-speed wind tunnel. The aluminum support blocks, which encase the main wing spar and serves as a ground for plunge and pitch springs, mount to Plexiglas plates that act as the ceiling and floor of the test section as shown in Figure 3.7a. Slots in the Plexiglas plates perpendicular to the flow allow the system to move in lateral plunge motion.

Figure 3.6: University of Washington low-speed wind tunnel

The air density is calculated using temperature and pressure measured by locally mounted barometer and thermometer. Instantaneous flow velocity in the test section is determined by a differential pressure gauge and U-tube manometer. The pressure gauge uses two pitot-static probes to determined the pressure difference between the static air at the entrance to the tunnel and air just up-stream of the model. The measurement equipment described in Section 3.2 were installed in the tunnel and used to track the motion of the system using the Jaguar system. Details about the tests conducted can be found in Chapters 4 and 7.

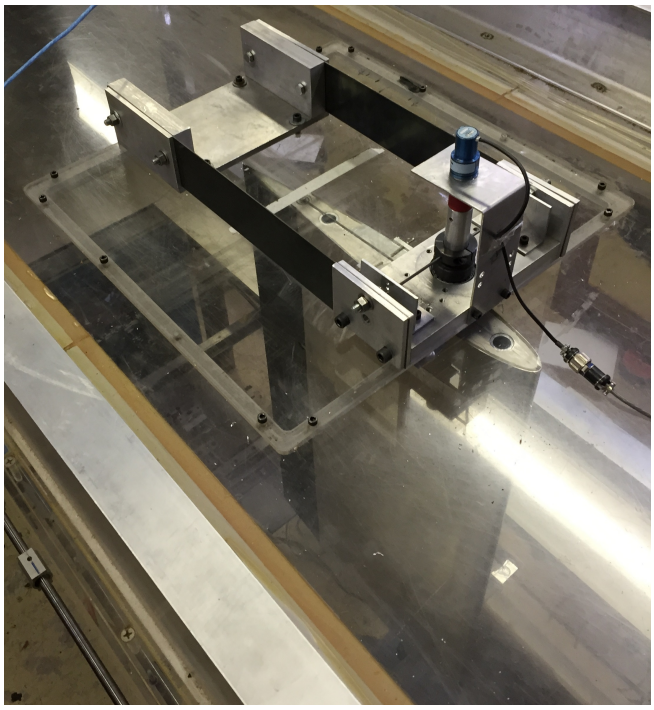

(a) Upper view of the experimental system mounted in the wind tunnel via support blocks

(b) View of the model in the test section with dampers attached

Figure 3.7: Experimental model mounted in UW low-speed wind tunnel (Note: In the tests presented in this thesis the dampers are not included)

Chapter 4

LINEAR FLUTTER ANALYSIS OF THE EXPERIMENTAL SYSTEM

To ensure accurate simulation of system behavior, two numerical models are utilized, one in the time domain, the other in the frequency domain. The frequency domain simulation used assumes motion is simple harmonic and applies Theodorsen's model of the unsteady aerodynamic contribution to the equations of motion. The time domain method utilizes a numerical integration scheme along with Roger's approximation of unsteady aerodynamics and is thus able to predict all types of motion: convergent, divergent, non-periodic, and simple harmonic. This chapter details the methodology and results of the linear simulations in the frequency and time domains and compares them to experimental results.

4.1 Linear Methodology - U-g Method

In a linear system, the flutter point is the dynamic pressure at which the system becomes dynamically unstable. The experimental system used in this research in the absence of freeplay is a linear system. The U-g method employed in the linear solution of the flutter problem converts the equations of motion to the form of a standard eigenvalue problem. By solving this eigenvalue problem at varying dynamic pressures and tracking the roots of the system, the flutter point of the system is found.

4.1.1 Equations of Motion in the Frequency Domain

In the frequency domain, motion is expressed in terms of a magnitude and a phase. As such, taking the general equations of motion for an aeroelastic system with

hysteretic damping:

$$\mathbf{M_s}\ddot{\mathbf{q}} + j\mathbf{G_{st}}\mathbf{K_s}\mathbf{q} + \mathbf{K_s}\mathbf{q} = \frac{1}{2}\rho U^2 \mathbf{A(jk)}\mathbf{q} \tag{4.1}$$

where the generalized displacements are a function of $j\omega$ and are defined as:

$$\mathbf{q} = \begin{Bmatrix} h \\ \alpha \\ \beta \end{Bmatrix} e^{j\omega t}, \quad \dot{\mathbf{q}} = j\omega \begin{Bmatrix} h \\ \alpha \\ \beta \end{Bmatrix} e^{j\omega t}, \quad \ddot{\mathbf{q}} = -\omega^2 \begin{Bmatrix} h \\ \alpha \\ \beta \end{Bmatrix} e^{j\omega t} \tag{4.2}$$

The equations in the frequency domain can be written in the form:

$$\left[-\omega^2 \mathbf{M_s} + \left[\mathbb{I} + j\mathbf{G_{st}}\right]\mathbf{K_s} - \frac{1}{2}\rho_\infty U_\infty^2 \mathbf{A(jk)}\right]\{\mathbf{q(j}\omega)\} = \{\mathbf{0}\} \tag{4.3}$$

where $\mathbb{I}$ represents the identity matrix and $\mathbf{q(j}\omega)$ refers to the complex vector of generalized displacements defined in Eq. 4.2.

4.1.2 Mathematical Approach

The linear U-g solution assumes the hysteretic damping model and assesses the stability of a given system by introducing an artificial damping variable g to the existing structural damping G_{st}. Noting that a system will oscillate in SHM given the right amount of damping, by determining the value of g needed for the system to oscillate in such a manner, the stability and flutter point of the system can then be found.

Introducing the artificial damping variable and multiplying through by the complex components of the state variables, the equations reduce to the form below, where all matrices have been previously defined.

$$\left[-\omega^2 \mathbf{M_s} + \left(\mathbb{I} + j\mathbf{G_{st}} + jg\mathbb{I}\right)\mathbf{K_s} - \frac{1}{2}\rho U^2 \mathbf{A(k)}\right]\{\mathbf{q(jk)}\} = \{\mathbf{0}\} \tag{4.4}$$

Dividing through by ω^2 (for $\omega \neq 0$), introducing the reduced frequency $k = \frac{\omega b}{U}$ and lumping terms, the system of equations can be presented as a standard, complex eigenvalue problem of the form:

$$[\mathbf{R}(\mathbf{k}) - \lambda \mathbf{S}] \{\mathbf{q}(\mathbf{jk}) = \{\mathbf{0}\} \tag{4.5}$$

where:

$$\mathbf{R}(\mathbf{k}) = -\mathbf{M_s} - \frac{1}{2}\rho_\infty \frac{b^2}{k^2} [\mathbf{A}(\mathbf{k})] \tag{4.6}$$

$$S = [\mathbb{I} + j\mathbf{G_{st}}][\mathbf{K}] \tag{4.7}$$

$$\lambda = \frac{1 + jg}{\omega^2} \tag{4.8}$$

With the eigenvalue problem defined, the process of determining the flutter point of the system can be summarized in the following loop:

- Prescribe a value of k
- Calculate $\mathbf{A}(\mathbf{jk})$, $\mathbf{R}$ and $\mathbf{S}$ matrices
- Solve the complex eigenvalue problem $[\mathbf{R} + \lambda \mathbf{S}] \{\phi\} = \{0\}$ for the eigenvalues λ_i of the system (for $i = h, \alpha, \beta$)
- Find and store parameters of the system

$$\text{for } Re(\lambda_i) > 0: \quad \omega_i(k) = \sqrt{\frac{1}{Re(\lambda_i)}}, \quad U_i(k) = \frac{\omega_i b}{k}, \quad g_i(k) = \frac{Im(\lambda_i)}{Re(\lambda_i)} \tag{4.9}$$

- Repeat at incremented reduced frequency, k

The stability of the system can be determined based on the sign and value of the artificial damping variable g. If g is positive, the system is unstable and damping must be added to the system to achieve SHM. If g is negative, the system is stable

and damping must be removed to achieve SHM. The point at which $g = 0$ is the flutter point of the system and the speed at which the system oscillates in SHM. This point can be visualized by generating plots of the stored values of U_i vs g_i and U_i vs ω_i and tracking their respective branches. The lowest speed at which a g branch becomes positive is the linear flutter speed, U_F, while the point on the corresponding frequency branch at U_F is the flutter frequency ω_F. Information about the nature of the instability and the intensity of the divergence can also be gained from these plots. This will be discussed in subsequent sections.

4.1.3 U-g Method Results for UW Experimental System

The results presented in this section for the linear flutter behavior of the UW experimental system were generated using codes developed at the University of Washington. The reader is directed to Ref [8] in which the codes are validated against Duke University data. Figure 4.1 shows the variation of the artificial damping parameter g and the corresponding frequency branches. The model predicts a flutter point of $18.52\frac{m}{s}$ at a frequency of $3.40Hz$. This point is located where the upper damping branch crosses the zero axis and becomes unstable. It can be seen that in the frequency domain a crossing of the zero damping axis corresponds to a coalescence of frequency branches. Because linear systems oscillate in a superposition of motions at any number of its natural frequencies, branch coalescence can often lead to energy transfer between two motions resulting in dynamic instability.

The U-g model also lends important information on the type of flutter that will occur. If as the airspeed is increased there is a gradual loss of damping in the unstable root as the flutter point is approached, the flutter will be mild. In this case, oscillations may diverge slowly and the approach to flutter during test would be indicated by gradual loss of overall damping as speed increases. If as airspeed is increased the

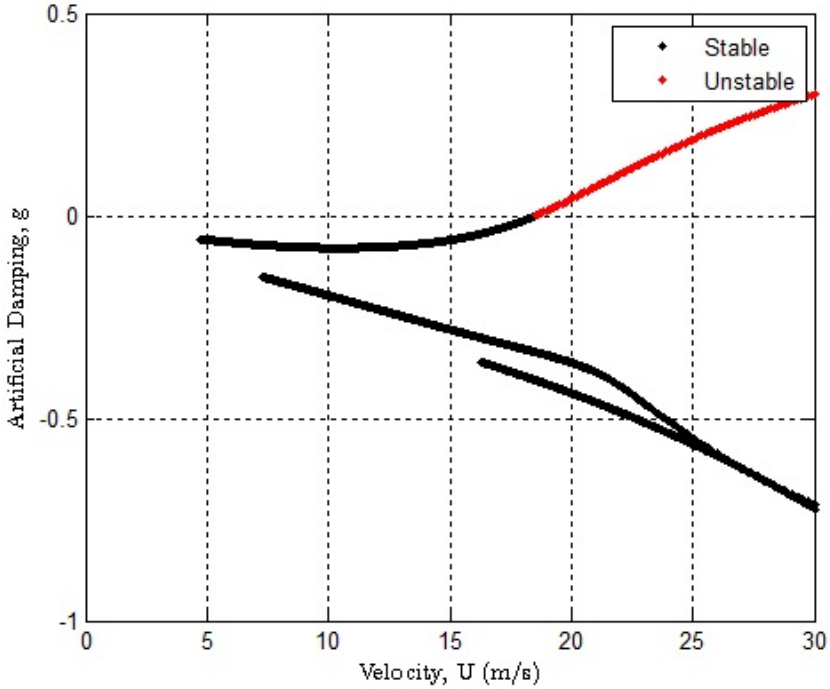

(a) Damping branch progression with speed

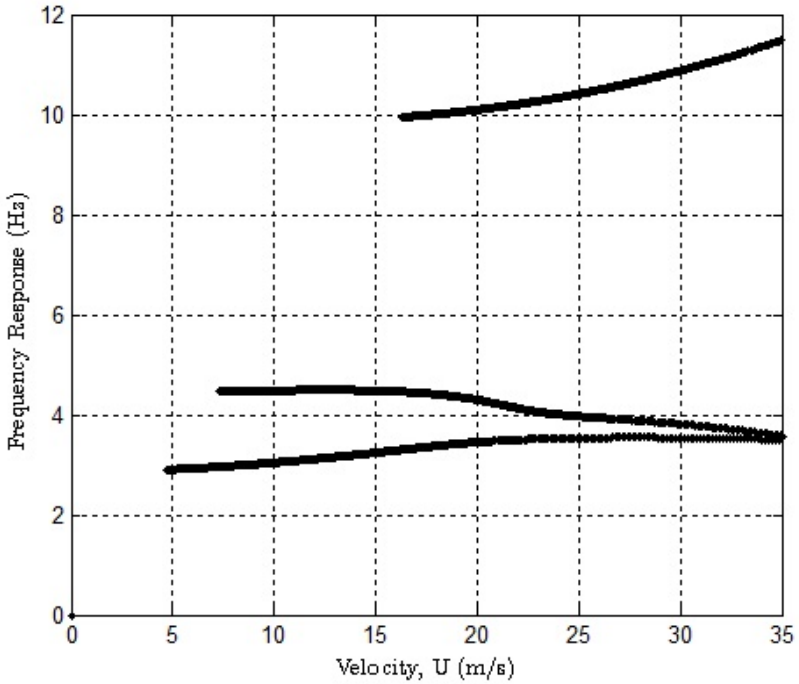

(b) Frequency branch progression with speed

Figure 4.1: U-g linear flutter results for the nominal UW System

system shows significant damping (negative artificial damping) then an abrupt loss of damping at the axis crossing, the flutter point is labeled explosive and can result in sudden total destruction of the experimental model. The results of the U-g simulations for the UW model show that the linear flutter will be relatively mild.

4.2 Linear Time Domain Model - Root Locus Method

The time domain simulation utilizes a linear time-invariant (LTI) state-space model of the equations of motion to predict system behavior. For the linear system, provided a LTI model, a simple eigenvalue analysis can be used to achieve these results. In considering system behavior other than simple harmonic, many techniques used in the frequency domain are no longer appropriate. First, the frequency domain simulations used a hysteretic damping model that is confined to SHM. It is thus replaced with a one-term viscous damping model such that the equations of motion become:

$$\left[-\omega^2\mathbf{M_s} + j\omega\mathbf{C} + \mathbf{K_s} - \frac{1}{2}\rho_\infty U_\infty^2 \mathbf{A(jk)}\right]\{\mathbf{q(jk)}\} = \{\mathbf{0}\} \tag{4.10}$$

4.2.1 Roger Approximation of Unsteady Aerodynamics

Second, the Theodorson method of approximating the aerodynamic contribution is also limited to SHM and is thus replaced by Roger's approximation method [11]. Unlike Theodorsen's method which utilized potential flow and complex variable theory, Roger's method expands the aerodynamic matrix into a rational function approximation series and uses least squares and Laplace transforms to determine the coefficients. This method is valid for all types of motion by the following rational. If for a known value of $j\omega$ $\mathbf{A(jk)}$ can be represented by a known Fourier transform valid on the $j\omega$ axis, by analytic continuation the approximation must also be valid in the complex plane governed by the Laplace transform $s = \sigma + j\omega$. Expanding the aerodynamic matrix:

$$\mathbf{A(j\omega)} = \mathbf{P_0} + j\omega\mathbf{P_1} - \omega^2\mathbf{P_2} + \sum_{n=1}^{l} \frac{j\omega}{j\omega + \beta_n}\mathbf{P_{n+2}} \tag{4.11}$$

The **P** matrices are determined via least squares fitting to tabulated data for known generalized aerodynamic matrices at a set of reduced frequencies. The β terms are referred to as aerodynamic poles, or lag roots and are preset to be within the range of $k_1 - k_n$. While the $A(jk)$ matrices are typically complex, the lag roots and P matrices are real valued. The expansion can now be extended to from the $j\omega$ axis to the complex plane via a Laplace transformation of the form.

$$\mathbf{A(s)} = \mathbf{P_0} + s\mathbf{P_1} + s^2\mathbf{P_2} + \sum_{n=1}^{4} \frac{s}{s + \beta_n}\mathbf{P_{n+2}} \tag{4.12}$$

The method of determined the P matrices is now detailed. If for a range of reduced frequencies $j\omega = jk\frac{U}{b}$ is known, the expansion can be written in the following form:

$$\mathbf{A(jk)} \approx \overline{\mathbf{P_0}} + jk\overline{\mathbf{P_1}} - k^2\overline{\mathbf{P_2}} + \sum_{n=1}^{4} \frac{jk}{jk + \overline{\beta_n}}\overline{\mathbf{P_{n+2}}} \tag{4.13}$$

where:

$$\begin{aligned}
\overline{\mathbf{P_0}} &= \mathbf{P_0} \\
\overline{\mathbf{P_1}} &= \mathbf{P_1}\frac{U}{b} \\
\overline{\mathbf{P_2}} &= \mathbf{P_2}\left(\frac{U}{b}\right)^2 \\
\overline{\mathbf{P_{n+2}}} &= \mathbf{P_{n+2}} \\
\overline{\beta_n} &= \beta_n\frac{b}{U}
\end{aligned} \tag{4.14}$$

Four lag terms are used in this numerical analysis ($l = 4$). The values of these terms that best suited the UW system are ($\beta_i = 0.05, 0.35, 0.875, 1.7$). The fraction in the summation is split into real and imaginary parts,

$$\frac{jk}{jk+\beta_n} = \frac{jk(\overline{\beta_n}-jk)}{(\overline{\beta_n}+jk)(\overline{\beta_n}-jk)} = \frac{k^2}{\overline{\beta_n}+k^2} + \frac{jk\overline{\beta_n}}{\overline{\beta_n}+k^2} \tag{4.15}$$

The real and imaginary tabulated data $Re(\mathbf{A}(\mathbf{k}))$ and $Im(\mathbf{A}(\mathbf{jk}))$ can be equated to the real and imaginary parts of the approximant as shown in the system of equations in matrix form $\mathbf{Lp} = \mathbf{R}$ as shown below for each term m, n.

$$\begin{bmatrix} 0 & -k_1^2 & \frac{k_1^2}{k_1^2+\overline{\beta_1}^2} & \frac{k_1^2}{k_1^2+\overline{\beta_2}^2} & \frac{k_1^2}{k_1^2+\overline{\beta_3}^2} & \frac{k_1^2}{k_1^2+\overline{\beta_4}^2} \\ k_1 & 0 & \frac{k_1^2\overline{\beta_1}}{k_1^2+\overline{\beta_1}^2} & \frac{k_1^2\overline{\beta_2}}{k_1^2+\overline{\beta_2}^2} & \frac{k_1^2\overline{\beta_3}}{k_1^2+\overline{\beta_3}^2} & \frac{k_1^2\overline{\beta_4}}{k_1^2+\overline{\beta_4}^2} \\ \vdots & \vdots & \vdots & \vdots & \vdots & \vdots \\ 0 & -k_N^2 & \frac{k_N^2}{k_N^2+\overline{\beta_1}^2} & \frac{k_N^2}{k_N^2+\overline{\beta_2}^2} & \frac{k_N^2}{k_N^2+\overline{\beta_3}^2} & \frac{k_N^2}{k_N^2+\overline{\beta_4}^2} \\ k_N & 0 & \frac{k_N^2\overline{\beta_1}}{k_N^2+\overline{\beta_1}^2} & \frac{k_N^2\overline{\beta_2}}{k_N^2+\overline{\beta_2}^2} & \frac{k_N^2\overline{\beta_3}}{k_N^2+\overline{\beta_3}^2} & \frac{k_N^2\overline{\beta_4}}{k_N^2+\overline{\beta_4}^2} \end{bmatrix} \begin{Bmatrix} \overline{P_1}_{m,n} \\ \overline{P_2}_{m,n} \\ \overline{P_3}_{m,n} \\ \overline{P_4}_{m,n} \\ \overline{P_5}_{m,n} \\ \overline{P_6}_{m,n} \end{Bmatrix} \approx$$

$$\approx \begin{Bmatrix} Re(A_{m,n}(jk_1)) - A_{m,n}(k_0=0) \\ Im(A_{m,n}(jk_1)) \\ \vdots \\ Re(A_{m,n}(jk_N)) - A_{m,n}(k_0=0) \\ Im(A_{m,n}(jk_N)) \end{Bmatrix} \tag{4.16}$$

The solution to the above system of equations yields the $\overline{P_N}_{m,n}$ element of the i_{th} $\mathbf{P}$ matrix for $i = 1 \rightarrow 6$. This is done through a least squares solution to the equation of the form:

$$\mathbf{L^T Lp} = \mathbf{L^T R} \tag{4.17}$$

With $\mathbf{p}$ now known, the $\mathbf{P_i}$ matrices can be found from the relations in 4.2.1. The accuracy of the Roger approximation matrices can be evaluated by plotting each m, n term against the tabulated data.

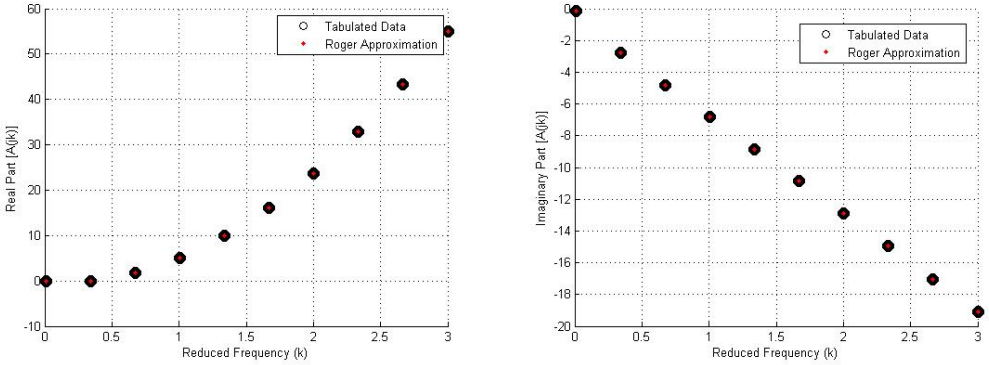

(a) $Re(A(1,1))$ Accuracy *(b)* $Imag(A(1,1))$ Accuracy

Figure 4.2: Sample of term-by-term fitting of the Roger approximation to tabulated data for the (1,1) term [8].

4.3 Generating the LTI State-Space Model

With the Roger approximation of the aerodynamic forces known, the equations of motion become:

$$\left(-\omega^2\mathbf{M_s} + j\omega\mathbf{C} + \mathbf{K_s} - \frac{1}{2}\rho_\infty U_\infty^2 \left[\mathbf{P_0} + j\omega\mathbf{P_1} - \omega^2\mathbf{P_2} + \sum_{n=1}^{4} \frac{j\omega}{j\omega + \beta_n}\mathbf{P_{n+2}}\right]\right)\{\mathbf{q(j}\omega)\} = \{\mathbf{0}\} \tag{4.18}$$

Transforming to the Laplace domain and lumping like s terms yields:

$$\left(s^2\overline{\overline{\mathbf{M}}} + s\overline{\overline{\mathbf{C}}} + \overline{\overline{\mathbf{K}}} - \frac{1}{2}\rho_\infty U_\infty^2 \sum_{n=1}^{4} \frac{s}{s + \beta_n}\mathbf{P_{n+2}}\right)\{\mathbf{q(s)}\} = \{\mathbf{0}\} \tag{4.19}$$

where

$$\begin{aligned}
\overline{\overline{\mathbf{M}}} &= \mathbf{M_s} - \frac{1}{2}\rho_\infty U_\infty^2 \mathbf{P_2} \\
\overline{\overline{\mathbf{C}}} &= \mathbf{M_s} - \frac{1}{2}\rho_\infty U_\infty^2 \mathbf{P_1} \\
\overline{\overline{\mathbf{K}}} &= \mathbf{M_s} - \frac{1}{2}\rho_\infty U_\infty^2 \mathbf{P_0}
\end{aligned} \tag{4.20}$$

With the equations of motion written in this form they can be converted to a Linear Time-Invariant (LTI) state space model of the form $\dot{\mathbf{x}} = \mathbf{A_p x}$ for numerical integration, where $\mathbf{A_p}$ refers to the system or plant matrix and $\mathbf{x}$ is the new vector of states to be solved for. The LTI model is created by defining the new state vectors as follows, where each vector is $3x1$:

$$\begin{aligned}
\{\mathbf{x_1}\} &= \{\mathbf{q}\} \\
\{\mathbf{x_2}\} &= s\{\mathbf{q}\} = s\{\mathbf{x_1}\} \\
\{\mathbf{r_1}\} &= \frac{s}{s+\beta_1}\{\mathbf{q}\} \Rightarrow s\{\mathbf{r_1}\} = -\beta_1\{\mathbf{r_1}\} + \{\mathbf{x_2}\} \\
\{\mathbf{r_2}\} &= \frac{s}{s+\beta_2}\{\mathbf{q}\} \Rightarrow s\{\mathbf{r_2}\} = -\beta_2\{\mathbf{r_2}\} + \{\mathbf{x_2}\} \\
\{\mathbf{r_3}\} &= \frac{s}{s+\beta_3}\{\mathbf{q}\} \Rightarrow s\{\mathbf{r_3}\} = -\beta_3\{\mathbf{r_3}\} + \{\mathbf{x_2}\} \\
\{\mathbf{r_4}\} &= \frac{s}{s+\beta_4}\{\mathbf{q}\} \Rightarrow s\{\mathbf{r_4}\} = -\beta_4\{\mathbf{r_4}\} + \{\mathbf{x_2}\}
\end{aligned} \tag{4.21}$$

The LTI is completed with a sixth equation for the acceleration of the system.

$$s\{\mathbf{x_2}\} = -\overline{\overline{\mathbf{M}}}^{-1}\overline{\overline{\mathbf{K}}}\{\mathbf{x_1}\} - \overline{\overline{\mathbf{M}}}^{-1}\overline{\overline{\mathbf{C}}}\{\mathbf{x_2}\} + \sum_{n=1}^{4}\frac{1}{2}\rho_\infty U_\infty^2 \overline{\overline{\mathbf{M}}}^{-1}\mathbf{P_{n+2}}\{\mathbf{r_n}\}$$

It can now be written in matrix form as shown in Eq 4.22 where $\mathbb{I}$ refers to the $3x3$ unit matrix and $\mathbf{0}$ to the $3x3$ null matrix of zeros. For a Roger approximation with four lag terms the plant matrix is an $18x18$ matrix and the vector of states is $18x1$.

$$
s\begin{Bmatrix} \{\mathbf{x_1}\} \\ \{\mathbf{x_2}\} \\ \{\mathbf{r_1}\} \\ \{\mathbf{r_2}\} \\ \{\mathbf{r_3}\} \\ \{\mathbf{r_4}\} \end{Bmatrix} = \begin{bmatrix} \mathbf{0} & \mathbb{I} & \mathbf{0} & \mathbf{0} & \mathbf{0} & \mathbf{0} \\ -\overline{\overline{\mathbf{M}}}^{-1}\overline{\overline{\mathbf{K}}} & -\overline{\overline{\mathbf{M}}}^{-1}\overline{\overline{\mathbf{C}}} & \frac{1}{2}\rho_\infty U_\infty^2 \overline{\overline{\mathbf{M}}}^{-1}\mathbf{P_3} & \frac{1}{2}\rho_\infty U_\infty^2 \overline{\overline{\mathbf{M}}}^{-1}\mathbf{P_4} & \frac{1}{2}\rho_\infty U_\infty^2 \overline{\overline{\mathbf{M}}}^{-1}\mathbf{P_5} & \frac{1}{2}\rho_\infty U_\infty^2 \overline{\overline{\mathbf{M}}}^{-1}\mathbf{P_6} \\ \mathbf{0} & \mathbb{I} & -\beta_1\mathbb{I} & \mathbf{0} & \mathbf{0} & \mathbf{0} \\ \mathbf{0} & \mathbb{I} & \mathbf{0} & -\beta_2\mathbb{I} & \mathbf{0} & \mathbf{0} \\ \mathbf{0} & \mathbb{I} & \mathbf{0} & \mathbf{0} & -\beta_3\mathbb{I} & \mathbf{0} \\ \mathbf{0} & \mathbb{I} & \mathbf{0} & \mathbf{0} & \mathbf{0} & -\beta_4\mathbb{I} \end{bmatrix} \begin{Bmatrix} \{\mathbf{x_1}\} \\ \{\mathbf{x_2}\} \\ \{\mathbf{r_1}\} \\ \{\mathbf{r_2}\} \\ \{\mathbf{r_3}\} \\ \{\mathbf{r_4}\} \end{Bmatrix} \tag{4.22}
$$

4.3.1 Mathematical Approach - Root Locus Method

In the time domain the linear case reduces to an eigenvalue problem as in the U-g method. In this case, however, a root locus analysis is used to track the roots of the system for incremented airspeeds U. For a specified atmospheric density and predetermined set of tabulated aerodynamic data $\mathbf{A}\left(\mathbf{j}(\mathbf{k_1} : \mathbf{k_N})\right)$, the process of determining the linear flutter speed can be summarized as follows:

- Set starting airspeed $U_{start} = \frac{\omega_{min} b}{k_N}$ for min structural frequency and max reduced frequency of the tabulated data
    - Begin loop of airspeeds
    - At given U, determine $\mathbf{P_n}$ matrices and subsequently the plant matrix $\mathbf{A_p}$
    - Determine complex eigenvalues $\lambda = \sigma + j\omega$ of $\mathbf{A_p}$ and plot them on the complex plane
    - Increment airspeed and repeat until U_{max}
- Track eigenvalue branches. The U at which an eigenvalue crosses the imaginary axis ($Re(\lambda) \geq 0$) corresponds to the linear flutter speed of the system U_F
- Find linear flutter frequency from imaginary part of critical eigenvalue where: $\omega_F = \frac{Im(\lambda)}{2\pi} Hz$

4.3.2 Root Locus Results for UW Experimental System

The results presented in this section for the UW experimental system were generated using codes developed at the University of Washington. The codes were validated using the results of Refs [1][2][3]. Figure 4.3 shows the movement of the eigenvalues for increasing airspeed. The speed at which the real part of any eigenvalue ($\lambda = \sigma + j\omega$) becomes positive is the flutter speed and the corresponding imaginary value is the flutter frequency.

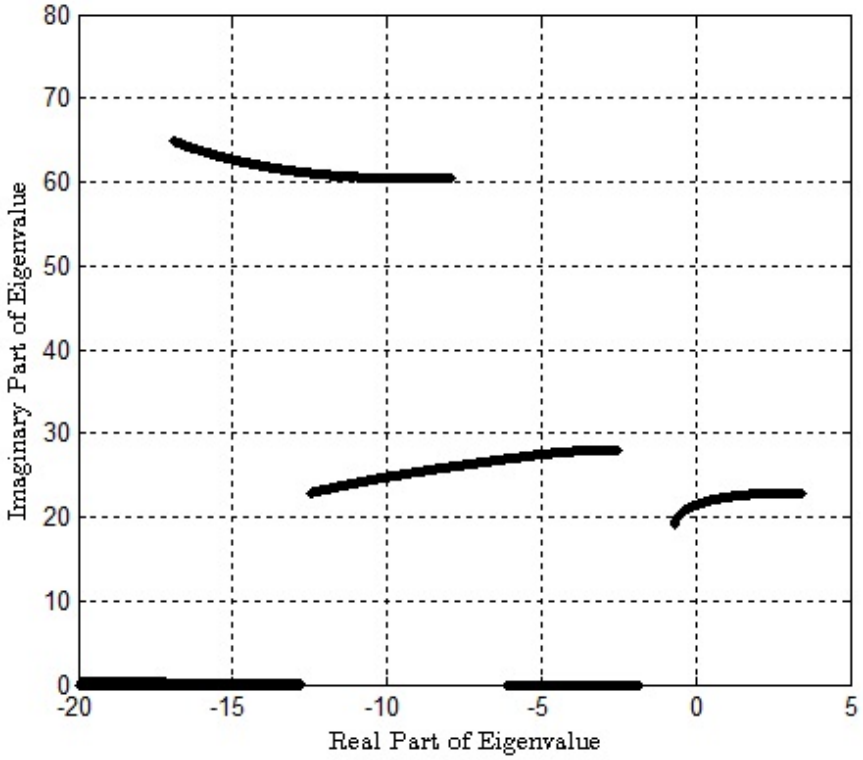

(a) Root locus plot of real and imaginary eigenvalue parts

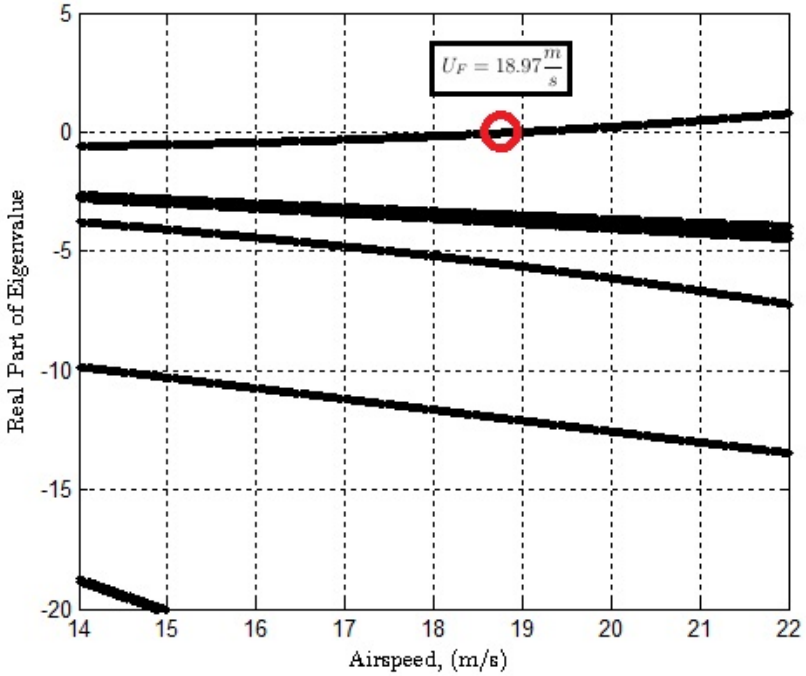

(b) $Re(\lambda) vs U$ showing linear flutter point

Figure 4.3: Root locus method results for the UW System

Table 4.1 summarizes the results of the root locus simulation along with those from the U-g method.

Table 4.1: Summary of Linear Flutter Results

U-g Method		**Root Locus Method**	
Speed, U_F	Frequency, ω_F	Speed, U_F	Frequency, ω_F
18.52 $\frac{m}{s}$	3.40 Hz	18.97 $\frac{m}{s}$	3.41 Hz

The results compare to within a fraction of a percent difference, building confidence on when flutter will occur in experimental testing.

4.4 Experimental Linear Flutter Test of the UW System

Experimental tests to determine the linear flutter speed and frequency of the UW system were conducted. Because the flutter point of the system can be very destructive, a method for extrapolating to the linear flutter point is used instead of taking the system to flutter. This method is summarized below.

- Starting at an established speed, U_{start}, incrementally increase the tunnel speed to prescribed test point speeds.
- At each test speed excite the structure in plunge to assess the stability of the system.
- With each excitation, capture the time history of selected responses.
- At each test point, use the time history output to determine the damping ratio of the least damped root by log decrement method at the given tunnel speed.
- Systematically plot damping ratios vs. tunnel speed at each test point observing their evolution.

As the system nears the linear flutter point there will be a loss in damping corresponding to impending instability. This loss in damping can be visualized in the minimum damping vs. velocity trend seen in Figure 4.5. Prior to complete loss in damping the test is terminated and the linear flutter point is extrapolated. The test conducted in the UW low speed wind tunnel was perhaps a bit "overzealous" and resulted in actual linear flutter from plunge excitation at $18.47\frac{m}{s}$. This test point along with the damping extrapolation is plotted in the following figure.

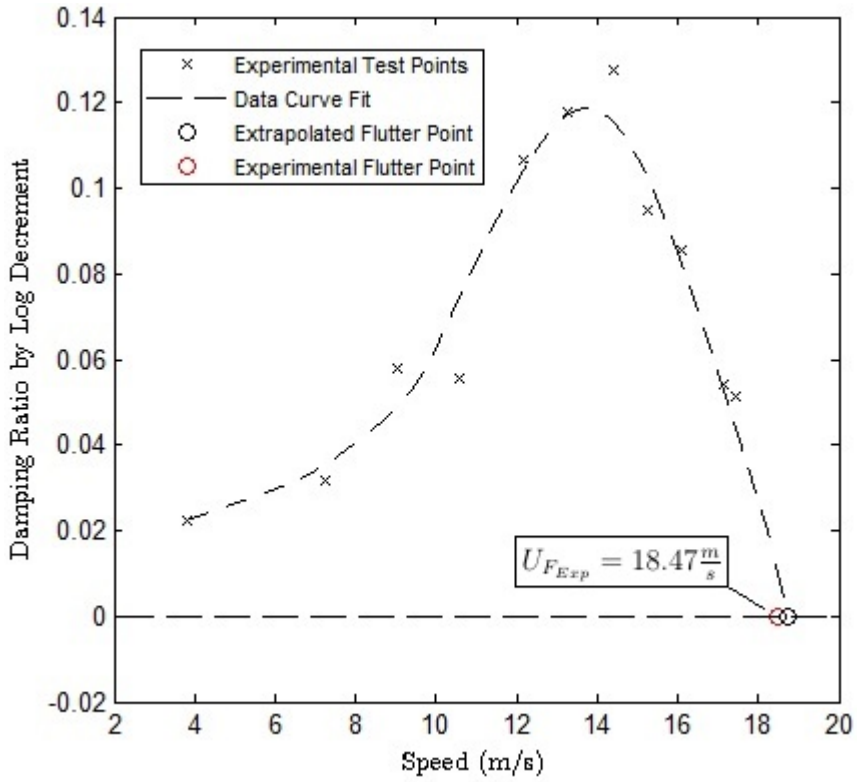

Figure 4.4: Linear flutter test of UW system: Averaged damping ratio ζ_h vs. tunnel speed

Here the averaged damping values over a series of three peaks of the plunge d.o.f. at each speed are used. The least damped root is used as the conservative value with the intention of avoiding linear flutter. It can be seen from the figure that the extrapolation from the damping points compares well to the actual flutter point of

the system. Further, the experimental test points compare well to predicted values as summarized in Table 4.2.

Table 4.2: Comparison of Experimental and Simulated Linear Flutter Results

	U-g Method	**Experimental**	**% Difference**
Speed, U_F	18.52 $\frac{m}{s}$	18.47 $\frac{m}{s}$	0.27%
Frequency, ω_F	3.40 Hz	3.7 Hz	8.1%

4.4.1 Causes of Discrepancy Between Linear Flutter Results

In actuality, higher correlation between predicted and experimental results is attainable. First, the experimental flutter speed is a small percentage higher than that presented, in that the system was stable at $18.47\frac{m}{s}$ prior to the excitation that led to flutter. It is likely that the magnitude of the excitation introduced additional dynamics, perhaps in the form of nonlinearities in damping or stiffness. Using the extrapolation point rather than the experimental test point is more reasonable and would yield higher correlation with analysis. Second, the fundamental assumption in Theodorsen unsteady aerodynamics is that the airfoil in question is thin and in free air. The airfoil used in the UW system is a NACA 0012, a thick airfoil. Studies of the effects of wall interference are presented in Ref [12]. It was found that the lift curve slope of the airfoil, $C_L\alpha$, was notably effected by its proximity to the wind tunnel walls.

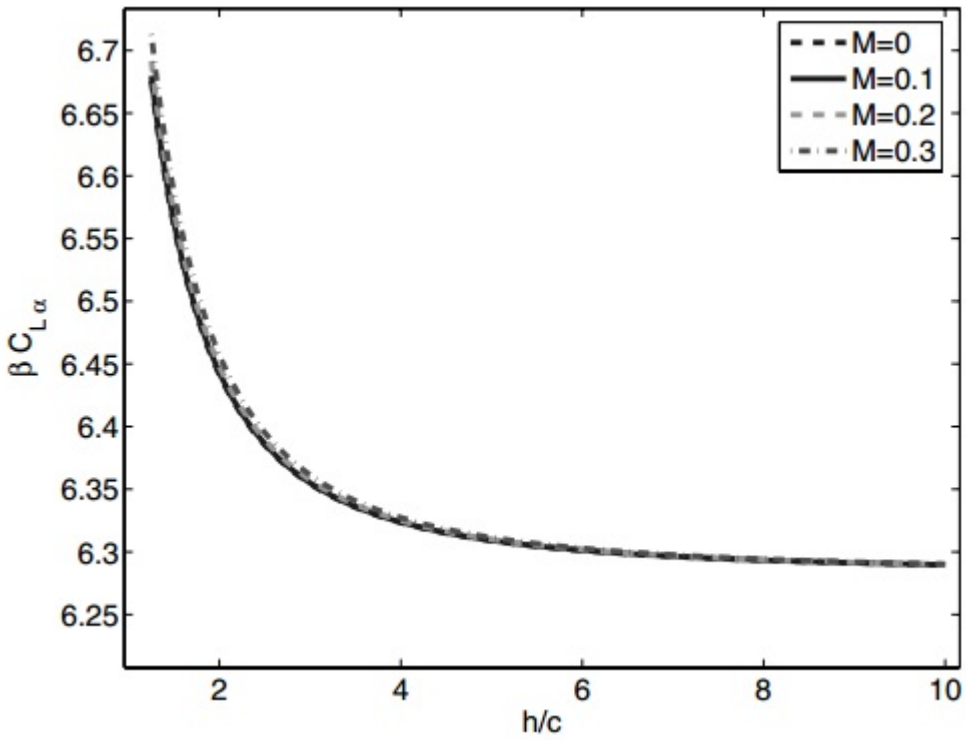

Figure 4.5: Corrected lift curve slope for steady flow over an airfoil with varying tunnel height[12]

This interference affects the aerodynamics predicted by Theodorsen and effectively reduces the predicted linear flutter speed of the system. Ideally a correction must be incorporated into the model that accounts for this effect. This can be accomplished via Computational Fluid Dynamic (CFD) simulations in conjunction with Modified Strip Theory [13] and is addressed by this work via sensitivity analysis.

Finally, throughout the test, although the system was in a linear configuration, it responded significantly to turbulent gusts in the tunnel. The response at high speeds when aeroelastic damping gets low can be compared to LCO like behavior although it was not. This oscillatory motion made data reduction of damping ratio values difficult and perhaps introduced an additional dynamic to the system unaccounted for in the mathematical models. This phenomenon is an important subject of future research.

4.5 Sensitivity Study on Structural Properties

Many of the measured structural properties of the UW experimental system are subject to uncertainty. This is due to the limited precision and accuracy measurement devices used and the presence of subtle nonlinearities in the system as discussed in Section 3.3.1. As such, a sensitivity study was conducted to assess the effect of the uncertainties of each property on the linear flutter speed and frequency of the system. Table 4.3 summarizes the nondimensional sensitivities of each property measured. All variations in each parameter yield linear trends in flutter speed and frequencies. The sensitivities associated with each variable are effectively the slope of the curve representing the variation of flutter speed and frequency with each respective property. This table shows that the total mass of the system as well as its pitch and plunge stiffnesses have the potential for significantly affecting the predicted linear flutter conditions.

Table 4.3: Nondimensional Parameter Sensitivities

	Flutter Speed $\left(\frac{m/s}{\%uncert.}\right)$	**Flutter Frequency** $\left(\frac{Hz}{\%uncert.}\right)$
m_{hh}	0.2706	-0.073
$m_{\alpha\beta}$	-0.0015	-0.0008
ζ_h	0.003	0.001
ζ_α	0.0016	-0.0032
ζ_β	-0.0023	-0.0003
K_h	-0.1992	0.0602
K_α	0.2966	0.0475
K_β	-0.0023	-0.0028
S_α	0.00	0.00
S_β	0.00	0.00
I_α	0.00	0.00
I_α	0.00	0.00
C_{L_α}	-0.056	-0.0054

Table 4.4 summarizes the uncertainty ranges associated with each property. The ranges are determined based on the precision of the measurement instruments, human

error in measuring the property values and on the data trends seen during system characterization trials. The effect of the inertia and static unbalance terms on the flutter point of the system are negligible and thus excluded.

Table 4.4: Estimated Property Uncertainties

System Property	**Uncertainty**
m_{hh}	$\pm 0.02\%$
K_h	$\pm 1\%$
K_α	$\pm 1\%$
K_β	$\pm 5\%$
ζ_h	$\pm 1\%$
ζ_α	$\pm 30\%$
ζ_β	$\pm 30\%$
C_{L_α}[12]	$\pm 7\%$

Chapter 5

NONLINEAR ANALYSIS OF EXPERIMENTAL SYSTEM IN THE FREQUENCY DOMAIN

With the introduction of control surface freeplay, the linear methodology becomes invalid as it is unable to account for the nonlinear terms that emerge in the equations of motion. As such, the describing function approach is used in the frequency domain to analyze the flutter point and LCO characteristics of the nonlinear system.

A sinusoidal-input describing function (Ref [14]) is a linearization technique used in cases of periodic motion where the output of the nonlinear element is modeled as a first-order periodic approximation driven at the input frequency. This is done with the assumption that the dominant motion of a nonlinear periodic component will be first-order sinusoidal. The first-order approximation is determined by taking the Fourier series expansion of the nonlinear component and keeping only the first-order terms. This process is detailed in the following sections and is explained in more detail in [14].

5.1 Mathematical Approach - Freeplay Nonlinearity

Control surface freeplay effects the stiffness term, K_β in the manner described by Figure 1.3. This relationship can also be presented in the piecewise function:

$$H_\beta = \begin{cases} K_\beta(\beta - \delta) & if|\beta| \geq \delta, \beta > 0, \\ K_\beta(\beta + \delta) & if|\beta| \geq \delta, \beta < 0, \\ 0 & otherwise \end{cases} \tag{5.1}$$

where δ represents half the size of the freeplay region. Assuming that the flap

rotation is dominantly first-order sinusoidal, it can be fairly modeled as:

$$\beta = \beta_0 \sin \omega t \tag{5.2}$$

The nominal rudder stiffness then becomes a function of the piecewise stiffness and the describing function of the freeplay nonlinearity.

$$K_{\beta,eq} = F_\delta K_\beta \tag{5.3}$$

The describing function, which accounts for the magnitude of the flap rotation relative to the size of the freeplay gap is the following piecewise function (Refs [1]-[3]&[14]):

$$F_\delta = \begin{cases} 0 & -\delta < \beta_s < \delta, \\ \frac{1}{\pi}(\pi - 2t - \sin 2t) & otherwise \end{cases} \tag{5.4}$$

where t is given by

$$t = \sin^{-1}\left(\frac{\delta}{\beta_s}\right) \tag{5.5}$$

The describing function represents the nondimensional equivalent linear flap stiffness which can be visualized in Figure 5.1. Below the freeplay threshold the equivalent stiffness is zero. As the flap magnitude increases, the effect of the freeplay region becomes increasingly negligible and the equivalent stiffness approaches the nominal stiffness, K_β.

The equations of motion are thus linearized by replacing the K_β term in the structural stiffness matrix by the equivalent stiffness term $K_{\beta,eq}$. Denoting the new stiffness matrix as $\mathbf{K_{DF}}$ the equations of motion can be presented in the form:

$$\left[-\omega^2\left(\mathbf{M_s} + \frac{1}{2}\rho_\infty \frac{b^2}{k^2}\mathbf{A(jk)}\right) + j\mathbf{G_{st}K_s} + \mathbf{K_{DF}}\right]\{\mathbf{q(j\omega)}\} = \{\mathbf{0}\} \tag{5.6}$$

As with the U-g method, this system of equations can be written as a complex eigenvalue problem of the form seen in Eq 4.5 where now:

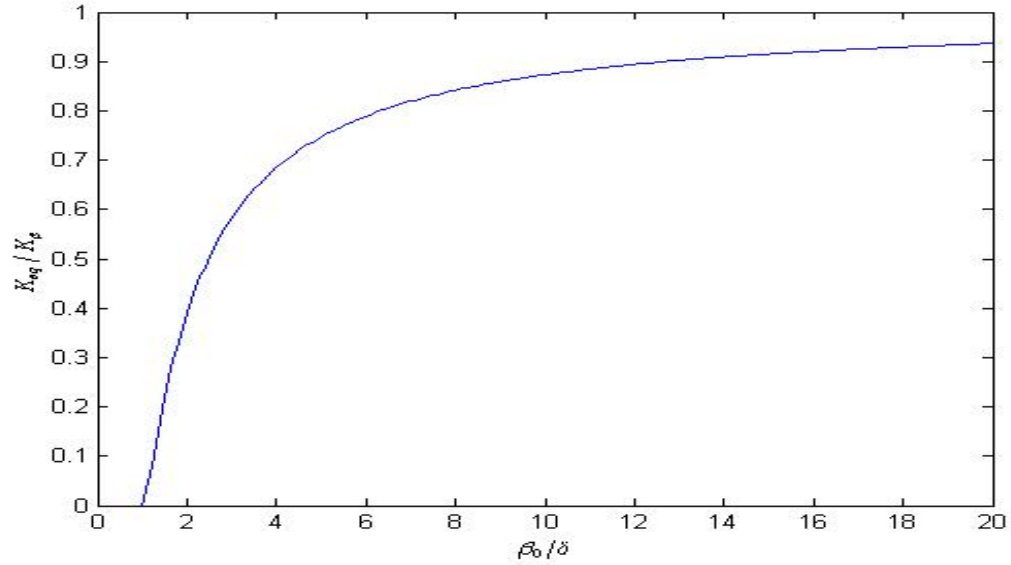

Figure 5.1: Nondimensional equivalent flap stiffness for the freeplay nonlinearity[3].

$$\mathbf{R}(\mathbf{k}) = j\mathbf{G_{st}}\mathbf{K_s} + \mathbf{K_{DF}}$$
$$\mathbf{S}(\mathbf{k}) = \mathbf{M_s} + \frac{1}{2}\rho_\infty \frac{b^2}{k^2}\mathbf{A}(\mathbf{jk}) \tag{5.7}$$
$$\lambda = \omega^2(1 + jg)$$

Because the system behavior is now dependent on dynamic pressure and flap amplitude, a modified approach from the U-g method is used. This method incorporates two loops through which g axis crossings and their associated U and ω values are stored. The procedure is summarized as follows:

- Begin outer loop of $\frac{\beta}{\delta}$ from 1 to set upper bound
- Calculate describing function F_δ and equivalent stiffness term $K_{\beta,eq}$
  - Begin inner loop of reduced frequency k from k_{max} to k_{min}
  - For each value of k generate and solve the complex eigenvalue problem

- For eigenvalues with $Real(\lambda_i) \geq 0$ determine g, ω and U values and store
- End inner loop

- Filter values from completed k-loop and pull out and store U, ω and k values at which the $g = 0$ crossings occur: all $g = 0$ solutions indicate possible LCOs
- Repeat at incremented $\frac{\beta}{\delta}$ value

Following the completion of these iterations, plots of the non-dimensional flap rotation vs U can be generated to analyze the LCO behavior and stability of the system. This will be discussed in a later section.

5.2 LCO Stability

As noted in Section 1.1, neighboring trajectories of a limit cycle are not necessarily closed and can spiral toward or away from the limit cycle. In traditional nonlinear dynamics, if the neighboring trajectories decay into the limit cycle amplitude, it is said to be stable. If the trajectories diverge from the limit cycle amplitude they are said to be unstable [5][15]. An alternative, and more intuitive method for analyzing LCO stability is used in this research. Three cases are run, one with the nominal damping value, one with a decrease in structural damping and one with an increase in structural damping. If for a certain LCO a decrease in damping results in an increase in LCO amplitude and an increase in damping results in a decrease in LCO amplitude then the limit-cycle is stable. The reverse is true for an unstable limit-cycle [5].

5.3 Describing Function Results for the UW System with Freeplay

The results presented in this section were generated using the nominal system's values provided in Section 3.1. They present the limit cycle amplitudes of their respective variables nondimensionalized by the size of the freeplay gap, δ_{FP}. In the

case of the plunge d.o.f. the amplitude is nondimensionalized by the half chord, b and δ_{FP}.

The results show that up to $5\frac{m}{s}$ the system is statically stable and any initial disturbance dies out. From $5\frac{m}{s}$ to roughly $5.5\frac{m}{s}$ two limit cycles exist. This can be seen well in the plot of rudder LCO amplitude and is faintly distinguishable in the plots of pitch and plunge. The lower portion corresponds to an unstable limit cycle and the upper to a stable limit cycle following the stability criterion in Section 5.2 as shown in the next Section. As such, in this speed region motion all neighboring trajectories will fall into the stable limit cycle at the amplitudes indicated. From $5.5\frac{m}{s}$ to $18\frac{m}{s}$ the describing function simulation predicts steady increase in all LCO amplitudes and frequency as more energy is injected into the system. Following $18\frac{m}{s}$ the simulation predicts exponential rise in all amplitudes corresponding to divergent flutter.

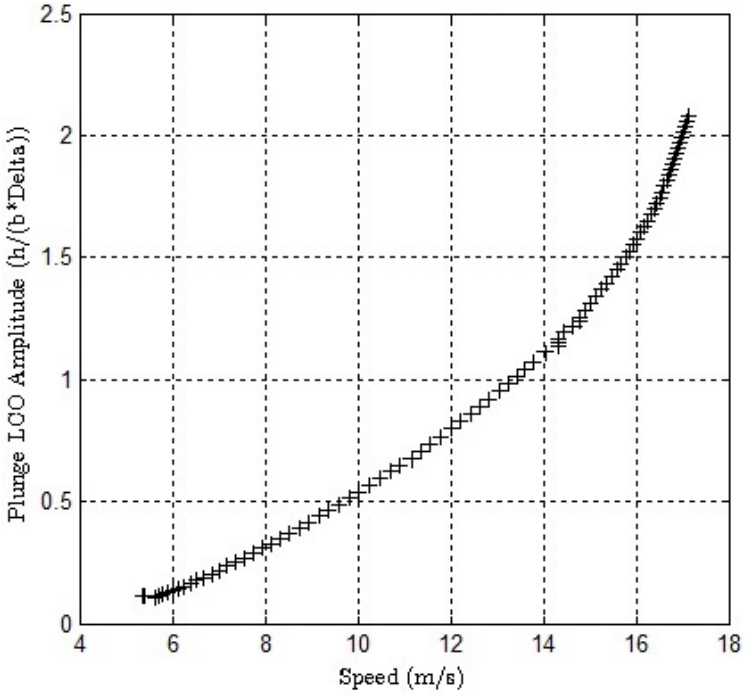

(a) Plunge amplitude

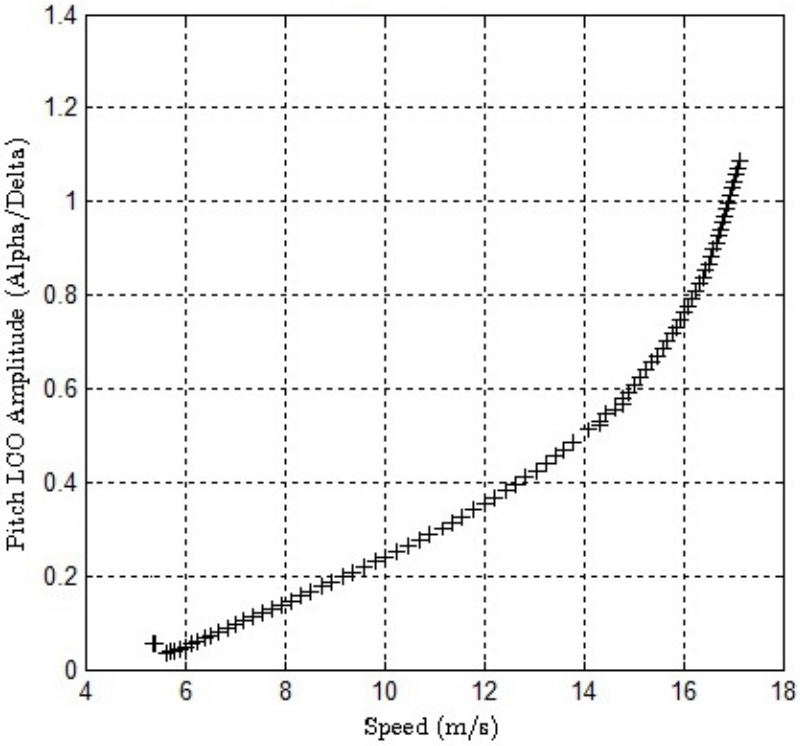

(b) Plunge amplitude

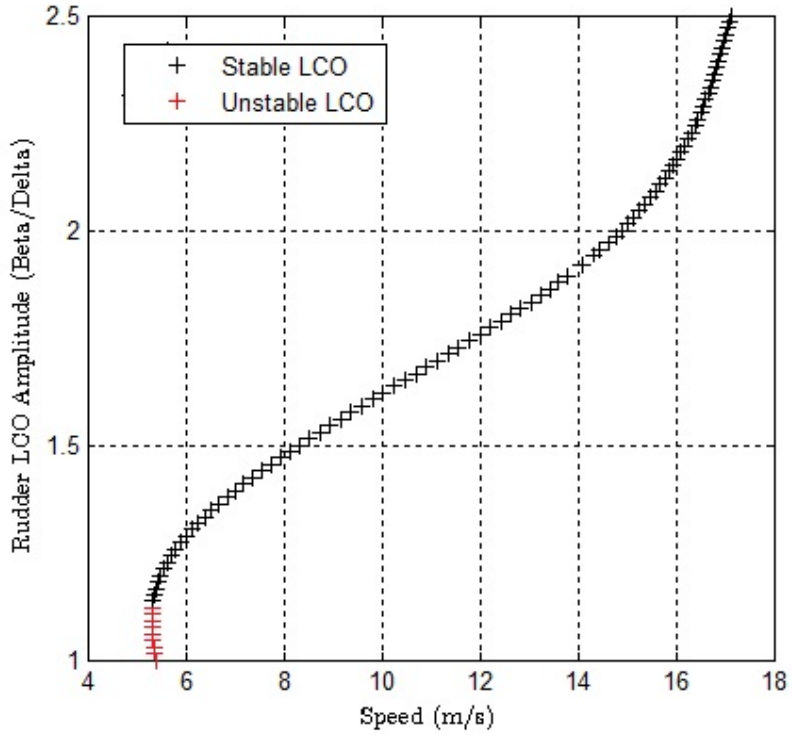

(c) Rudder amplitude

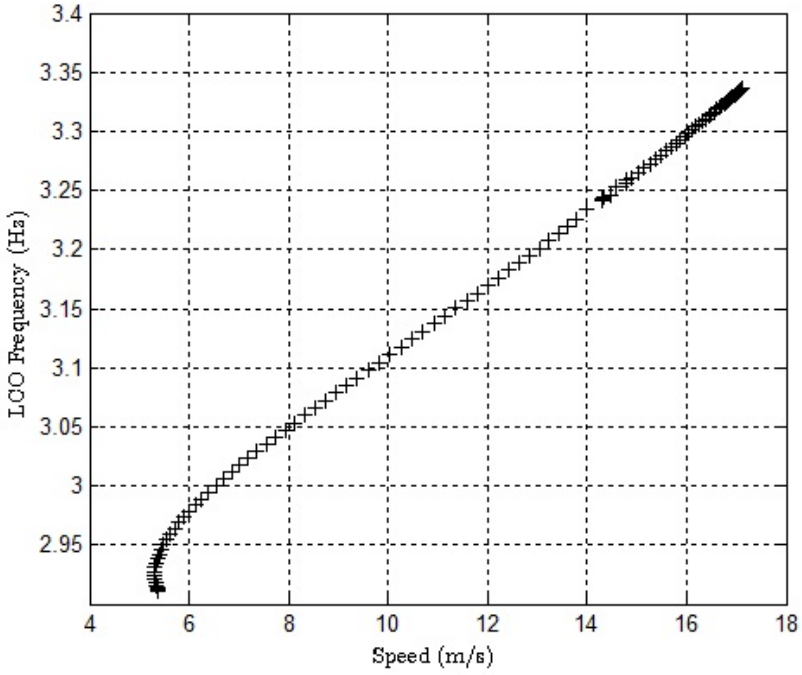

(d) LCO frequency

Figure 5.2: Non-dimensionalized LCO amplitudes as determined by frequency domain simulations

5.3.1 Limit Cycle Stability of the Nonlinear System

As explained in Section 5.2, the stability of a given limit cycle can be determined practically using the structural damping of the system. Figure 5.3 shows three curves of rudder LCO amplitudes for varying values of structural damping. LCO amplitudes above roughly 1.1 correspond to stable limit cycles while those below 1.1 correspond to unstable limits. Limit cycles above 1.1 are stable because an increase in damping results in a decrease in LCO amplitude. The reverse is true for the unstable limit cycles.

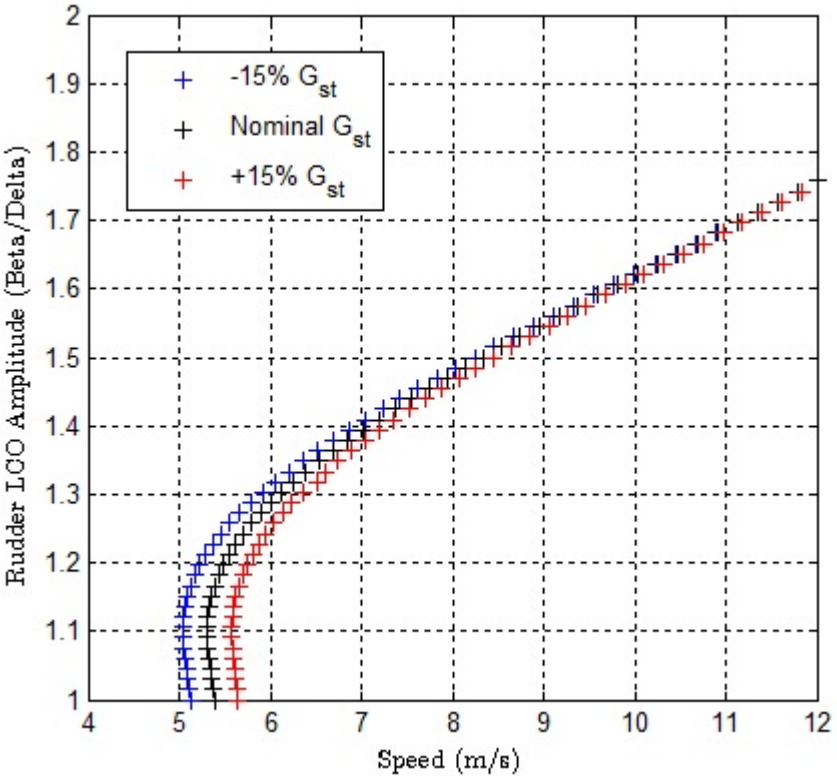

Figure 5.3: LCO Stability of UW system based on variation in the structural damping matrix, G_{st}

Chapter 6

NONLINEAR ANALYSIS OF EXPERIMENTAL SYSTEM IN THE TIME DOMAIN

Once freeplay is introduced, eigenvalue analysis is no longer a viable means of modeling the aeroelastic system. A numerical time integration solution method is thus used as it's capable of predicting types of motion other that simple harmonic in the presence of nonlinearities.

6.1 Mathematical Approach - Freeplay

The nonlinear methodology expands on the LTI model derived in the linear portion of this report at which point the system dynamics were represented by Eq 4.22 of the form $\dot{\mathbf{x}} = \mathbf{A_p x}$.

The hinge stiffness nonlinearity is incorporated in the same fashion as in the describing function method as a piecewise restoring force which can be added to the LTI model as such:

$$\left(s^2\overline{\overline{\mathbf{M}}} + s\overline{\overline{\mathbf{C}}} + \overline{\overline{\mathbf{K}}} - \frac{1}{2}\rho_\infty U_\infty^2 \sum_{n=1}^{4} \frac{s}{s+\beta_n}\mathbf{P_{n+2}} \right) \{\mathbf{q(s)}\} = \{-\mathbf{f}_\beta\} \tag{6.1}$$

where $\mathbf{f}_\beta$ and $\mathbf{H}_\beta$ are defined:

$$\mathbf{f}_\beta = \begin{Bmatrix} 0 \\ 0 \\ H_\beta \end{Bmatrix} \quad , \qquad H_\beta = \begin{cases} K_\beta(\beta - \delta) & if|\beta| \geq \delta, \beta > 0, \\ K_\beta(\beta + \delta) & if|\beta| \geq \delta, \beta < 0, \\ 0 & otherwise \end{cases} \tag{6.2}$$

Following the process for defining the first order state vectors of the LTI model summarized in Section 4.3 where the sixth equation in this case is,

$$s\{\mathbf{x_2}\} = -\overline{\overline{\mathbf{M}}}^{-1}\overline{\overline{\mathbf{K}}}\{\mathbf{x_1}\} - \overline{\overline{\mathbf{M}}}^{-1}\overline{\overline{\mathbf{C}}}\{\mathbf{x_2}\} + \sum_{n=1}^{4}\frac{1}{2}\rho_\infty U_\infty^2\overline{\overline{\mathbf{M}}}^{-1}\mathbf{P_{n+2}}\{\mathbf{r_n}\} - \overline{\overline{\mathbf{M}}}^{-1}\{\mathbf{f}_\beta\} \quad (6.3)$$

the state space representation becomes one of the form:

$$\dot{\mathbf{x}} = \mathbf{A_p}\mathbf{x} + \mathbf{B} \quad (6.4)$$

where $\mathbf{A_p}$ remains from Eq 4.22 and $\mathbf{B}$ is defined as:

$$\mathbf{B} = \begin{Bmatrix} \{\mathbf{0}\} \\ -\overline{\overline{\mathbf{M}}}^{-\mathbf{1}}\{\mathbf{f}_\beta\} \\ \{\mathbf{0}\} \\ \{\mathbf{0}\} \\ \{\mathbf{0}\} \\ \{\mathbf{0}\} \end{Bmatrix}_{18x1} \quad (6.5)$$

With the state-spaced model defined the LCO behavior of the system is determined as follows:

- Begin loop over flight speeds from U_{start} to a value expected to exceed the flutter speed
- At each airspeed perform a Runge-Kutta numerical integration using MATLAB's *ode*45
    - Specify an initial condition and initiate the integration over a prescribed time vector
    - At each time step track the system's current β value and use it to determine the $\mathbf{B}$ matrix and subsequently the systems next position

  - Proceed until the system has damped out, reached steady-state oscillation (LCO), or diverged

- In the case of LCO, extract the amplitude of motion of each d.o.f. and nondimensionalize with the size of the freeplay gap (δ)
- Plot normalized results vs. airspeed, U, for analysis

Note that the discontinuity in the freeplay function excites high harmonics and must be carefully handled during the integration (Ref [1]). It is not clear, however how precisely the time domain model represents the physical system here regarding the torque/rotation changes around "corners", which may be smoother. For first order effect standard Runge-Kutta integration with adaptive step size was used.

6.2 Time Domain Results for the UW System with Freeplay

As before, the results presented are those for the nominal system and present the nondimensionalized limit cycle amplitudes of the respective degrees of freedom. For comparison the time simulations are plotted along with the describing function results. These results are summarized in Figure 6.1. Multiple initial conditions were investigated to determine their effect on the LCO distributions. Two initial conditions are presented here to show the effect of plunge excitation - the excitation method used in experimental testing. The two initial displacements are $20cm$ simulating a physical push to the system and 2 cm simulating turbulent excitation in the tunnel. The frequency, however, is unaffected by the magnitude of the perturbation from steady state.

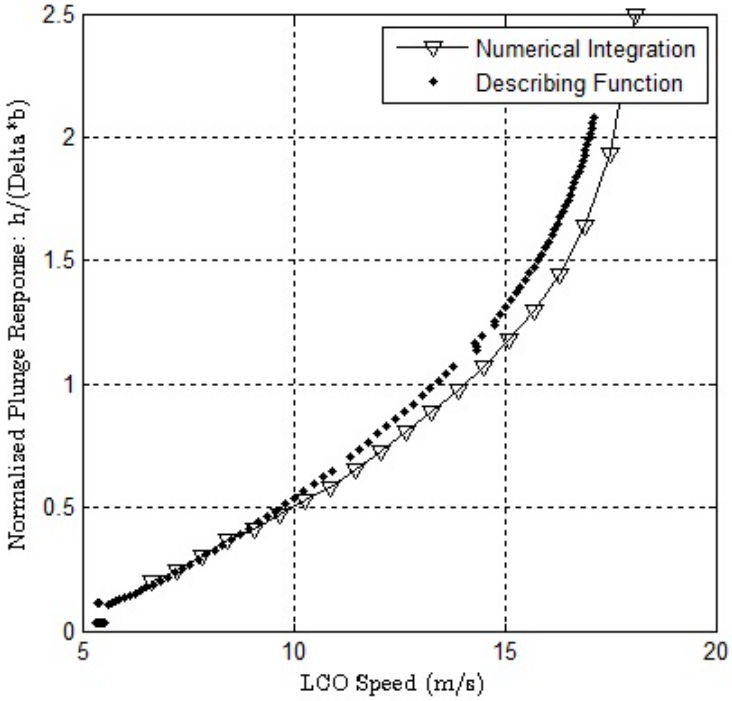

(a) Plunge amplitude

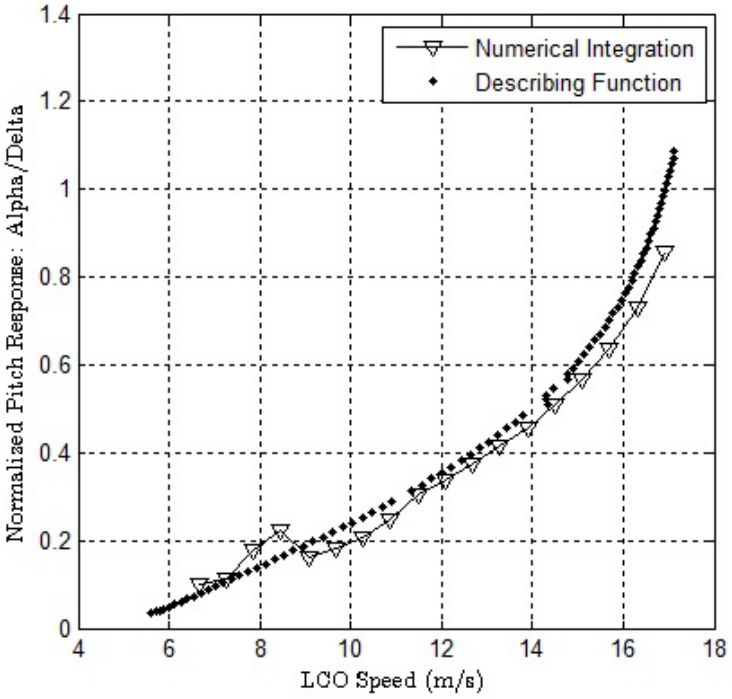

(b) Pitch amplitude

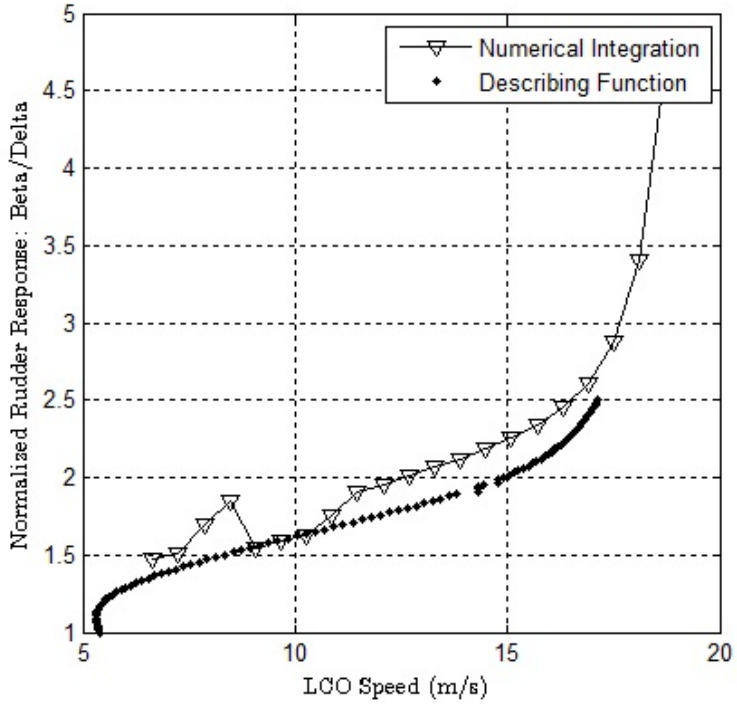

(c) Rudder amplitude

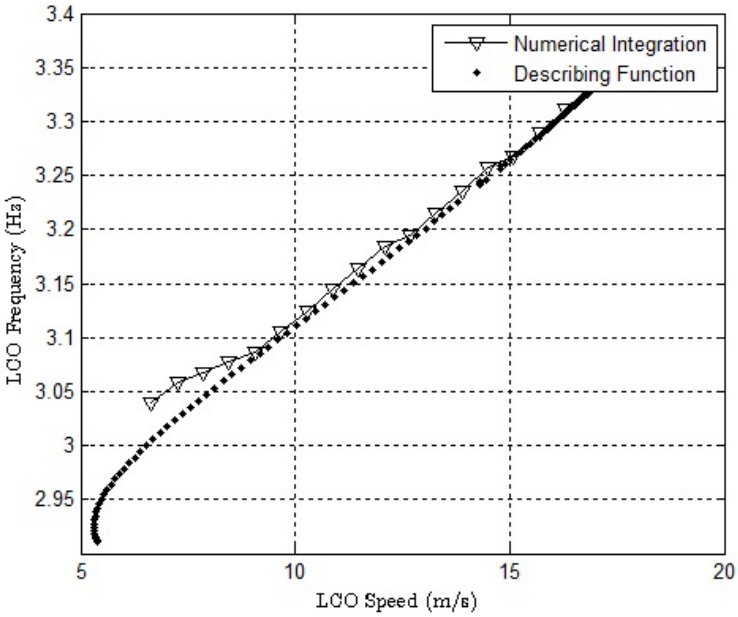

(d) LCO Frequency

Figure 6.1: Comparison of non-dimensionalized LCO amplitudes as determined by frequency and time domain simulations

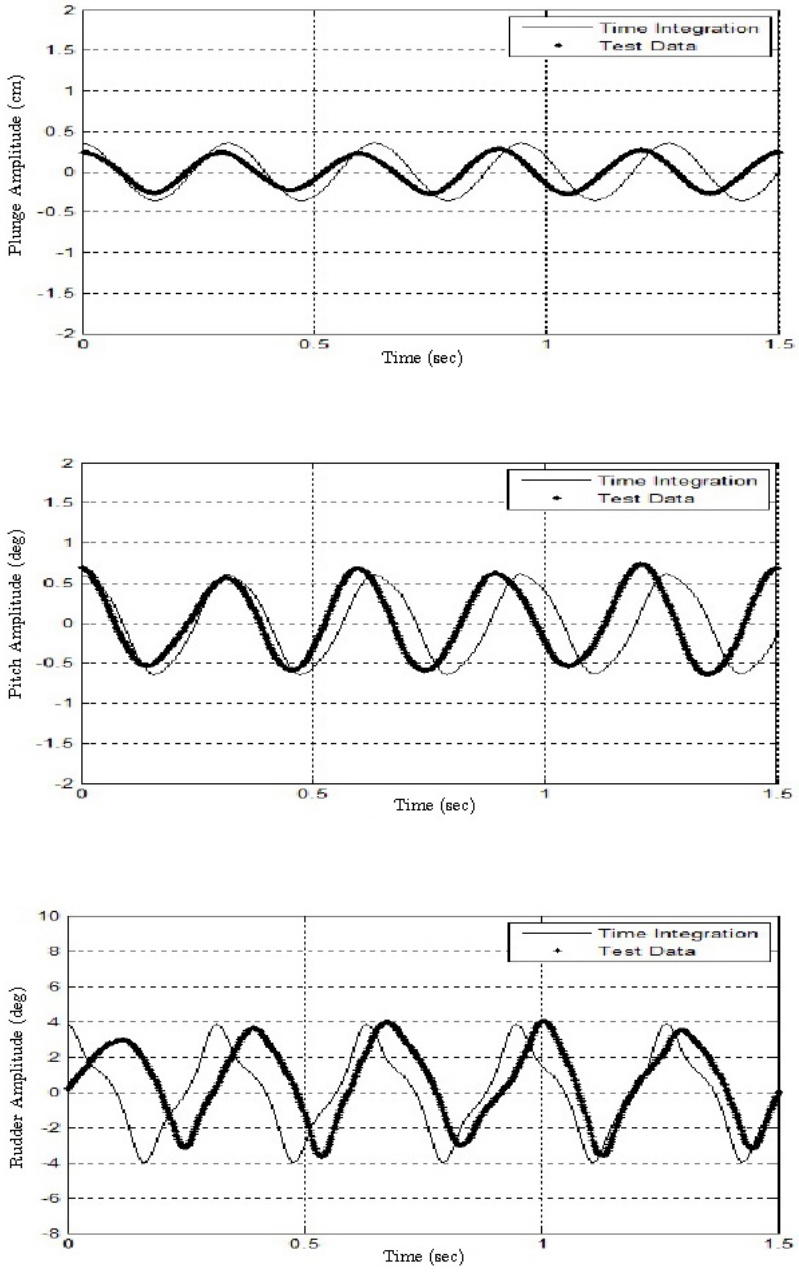

Figure 6.2: Predicted and measured limit cycle oscillation amplitudes for flow velocity of $11.26\frac{m}{s}$ and initial displacement of $2cm$.

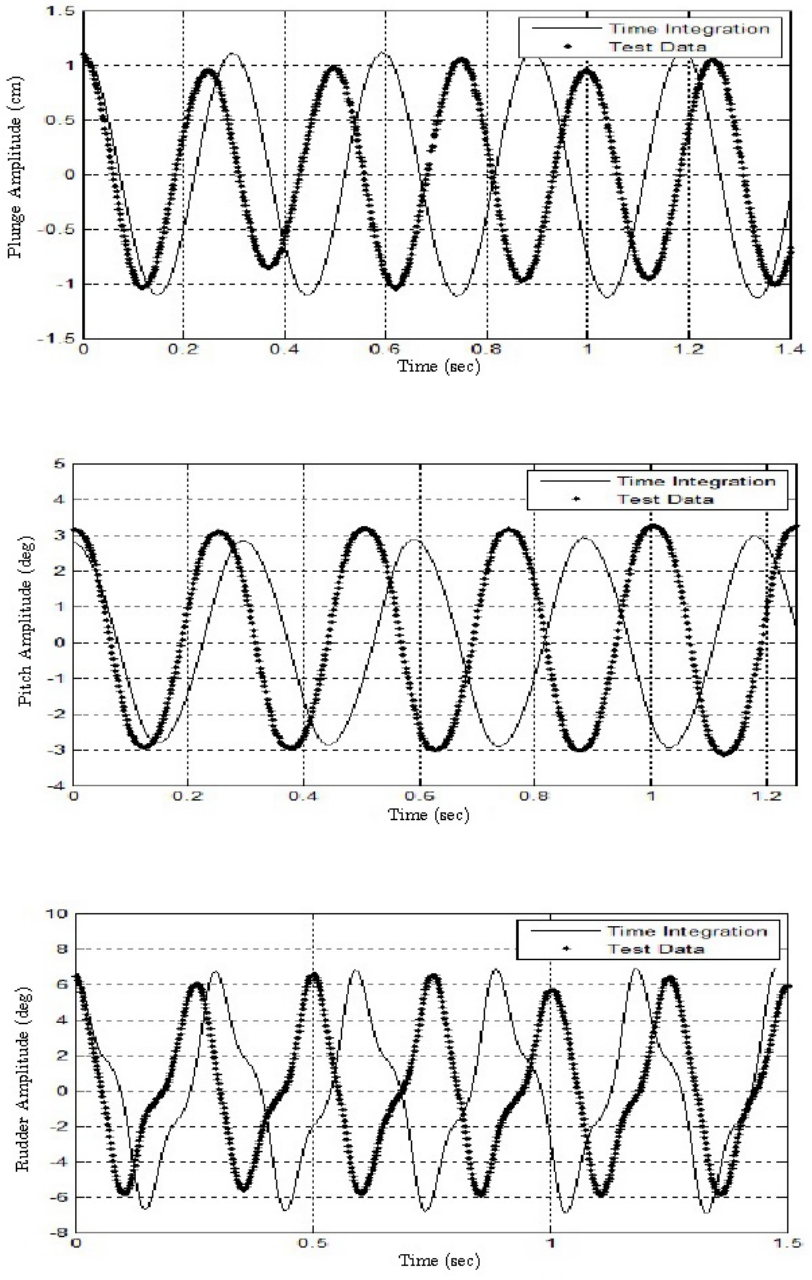

Figure 6.3: Predicted and measured limit cycle oscillation amplitudes for flow velocity of $17.06\frac{m}{s}$ and initial displacement of $2cm$.

Figures 6.2 and 6.3 provide a comparison of experimental and numerical time histories. Similar to the results of Refs [2][3], there is a discrepancy in LCO frequency that grows roughly linearly with flow velocity. At the test point at $11.26\frac{m}{s}$ the frequency is predicted quite well. However at the second test point at $17.06\frac{m}{s}$ the frequency of oscillation varies by 12%. It is suspected that this difference in frequency is spurred by tunnel turbulence and unpredicted system dynamics. Overall the results shows good correlation between qualitative and quantitative behavior.

Chapter 7

EXPERIMENTAL LIMIT CYCLE TESTS OF THE UW SYSTEM WITH FREEPLAY

Tests for measuring and analyzing the limit cycle behavior of the system with freeplay were conducted in a similar fashion to the those previously described for the linear system. The test procedure can be summarized as follows:

- Using rudder freeplay screws (Fig 3.5c), set desired freeplay gap as determined by the rudder RVDT output.
- Incrementally increase the tunnel speed to test points prescribed in the test matrix
    - At each flow speed, observe system behavior. If no limit cycle occurs, excite the structure via a push to the main wing spar and see if the initial condition causes an LCO to occur.
    - Once an LCO emerges, capture the limit cycle magnitudes via the Jaguar system and save time histories.
- Continue until the linear flutter speed is approached and limit cycle magnitudes are large enough to warrant test termination

At velocities lower than $5\frac{m}{s}$, the system was stable and no limit cycles occurred. At speeds between $5\frac{m}{s}$ and $7\frac{m}{s}$, excitation was needed to cause the system to fall into low frequency, low magnitude oscillation. As the tunnel speed was increased beyond $7\frac{m}{s}$, the turbulence in the tunnel provided sufficient excitation to cause the nonlinear

system to oscillate in LCO. With increase in flow speed the LCO magnitudes and frequency of oscillation increased as the data illustrates.

After data collection, the magnitudes of each d.o.f. at each test point were extracted from the time histories and plotted against simulation curves. The results are presented in Figure 7.1. Three freeplay gap sizes were investigated to determine if any effects on LCO amplitude exist. Because the data points are normalized with respect to the freeplay gap size, little variation between test cases is expected. Slight variation in amplitude can be seen between gap sizes. This is likely due to tunnel turbulence and other dynamic phenomenon not accounted for in the simulations. LCO frequencies vary slightly from predicted as expected due to discrepancies in model frequency predictions explained in Section 3.2. In order to more accurately model the system frequencies, a better understanding of its dynamical behavior in the tunnel must be achieved. Overall experimental amplitudes follow predicted trends very well, to the level of accuracy or better than those measured for the Duke system. Note the better consistency between the normalized $\frac{\beta}{\delta}$, $\frac{\alpha}{\delta}$, $\frac{h}{b\delta}$ values measured for the larger gap sizes of 2.3 deg and 3.5 deg compared to the $\delta_{FP} = 1.2$ deg results. The LCO test results with the smaller gap are more influenced by the magnitude of oscillation due to turbulence in the tunnel.

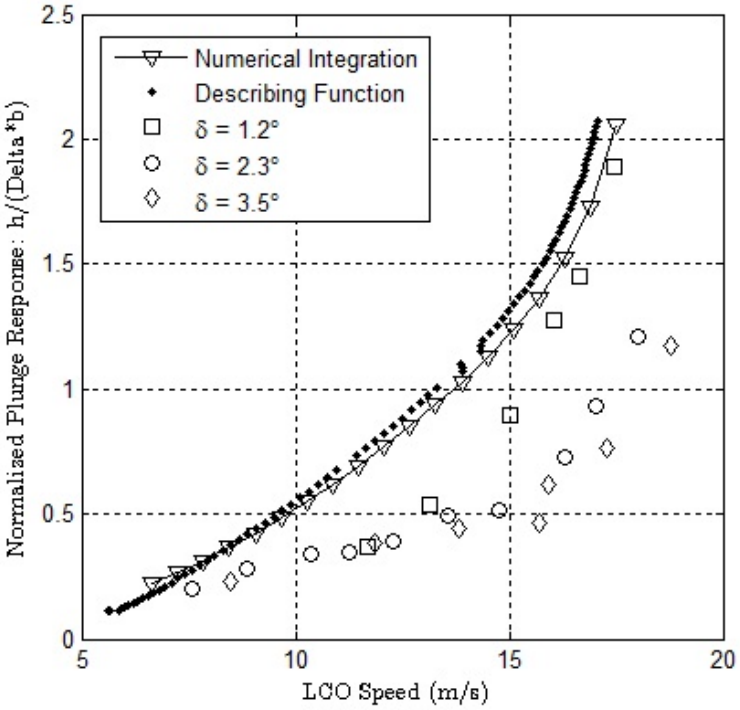

(a) Plunge amplitude

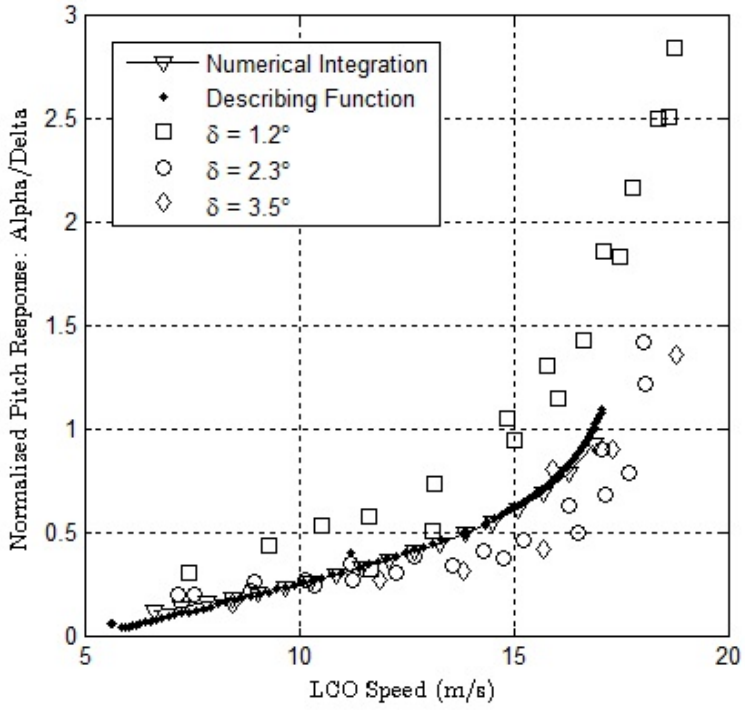

(b) Pitch amplitude

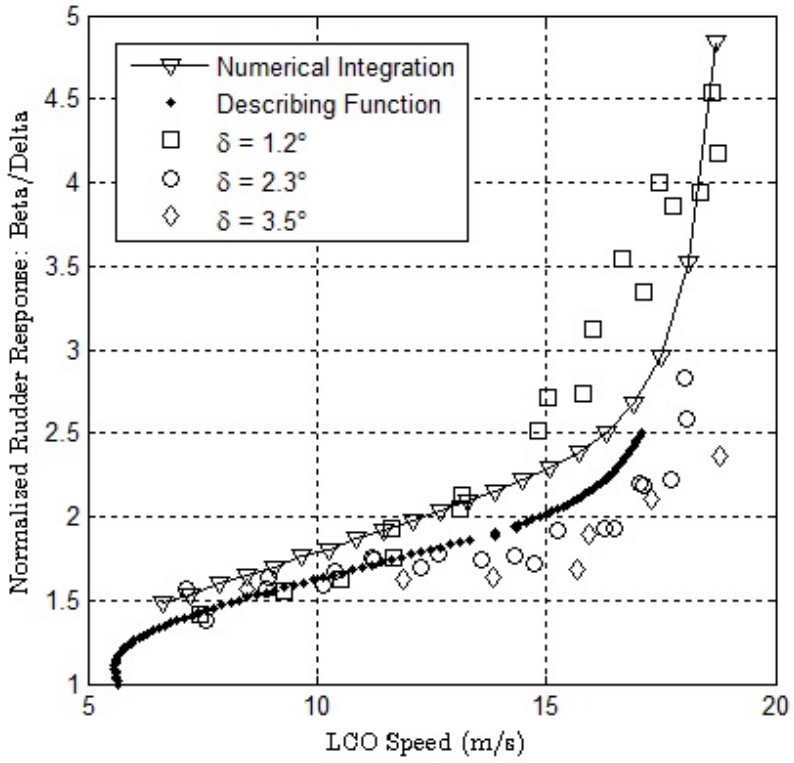

(c) Rudder amplitude

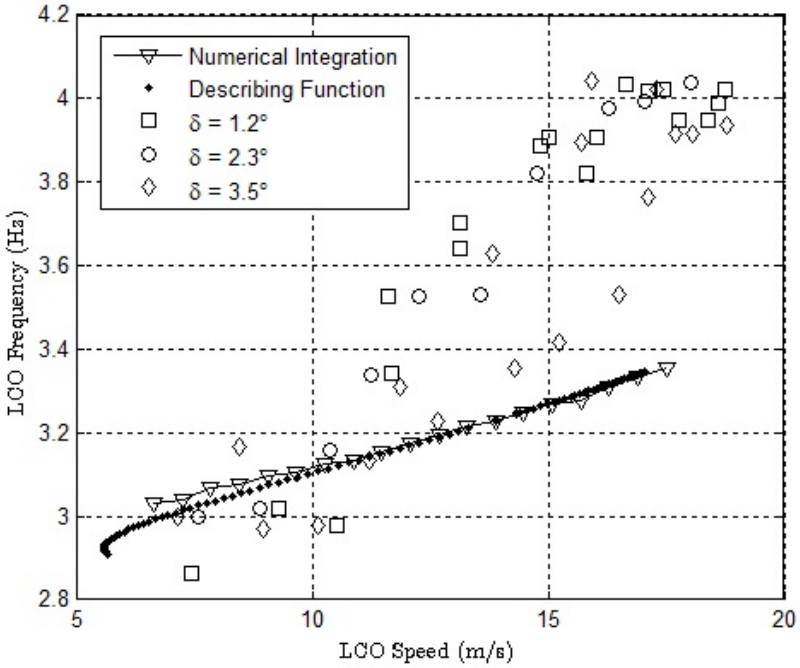

(d) LCO Frequency

Figure 7.1: Comparison of non-dimensionalized LCO amplitudes as determined by frequency and time domain simulations

Chapter 8
CONCLUSIONS

This thesis details the development and results of analytical and numerical simulations of linear and nonlinear behavior of the University of Washington experimental 3 d.o.f. 2D aeroelastic system. Equations of motion governing the behavior of the system were created using structural dynamics, Lagrangian theory and Theodorsen and Roger aerodynamics. Their results were validated against precedent data for Boeing and Duke research groups. The structural characteristics and modal frequencies of the system were determined by various methods and fine-tuned to ensure good comparison between measured values and those predicted by CAD and mathematical models.

Frequency domain simulations were created by reducing the equations of motion into a standard U-g eigenvalue problem. The eigenvalues, or roots of the system are tracked with varying flight speed to determine linear flutter qualities. Time domain simulations used a Roger approximation of the unsteady aerodynamics and analyzed the system by placing the equations of motion in the form of a LTI state-space model. The linear flutter speed and frequency determined via frequency and time domain simulation were compared to extrapolated and measured values using trends in damping ratio over a sweep of flight speeds. The results showed good correlation between measured and predicted - a difference of 10%.

Nonlinearities were incorporated into the frequency domain mathematical models via the describing function method, in which the nonlinear term was reduced to a first-order approximation. The nonlinear system responds in the form of limit cycle oscillation, close trajectories in phase space. The amplitudes of these LCOs were pre-

dicted numerically by the describing function method. These amplitudes were also approximated in the time domain by direct time integration of the LTI model using a standard Runga-Kutta integration scheme. Both methods show gradual increase in LCO amplitudes for all degrees of freedom as flight speed increases. Experimental flutter tests were conducted in the UW low speed wind tunnel with the system set to a variety of different freeplay gaps ranges. For each test case, flight speed was incrementally increased until LCO was achieved. At each tunnel speed, LCO amplitudes and frequencies were recorded for each d.o.f. using the Jaguar data acquisition system. Predicted limit cycle amplitudes from both methods were compared to experimental data points showing good correlation overall. Despite good agreement between results, the model's aerodynamic approximation has a degree of inaccuracy due to its inability to account for airfoil thickness and wall interference. It is the writer's hope that these results be useful in the continual advancement of the field of aeroelasticity at the University of Washington.

8.1 Future Work

This research was by no means inclusive or complete. Before the approximation techniques outlined in this thesis can be truly relied upon and expanded to incorporate further elements or nonlinearities, the following issues must be addressed.

- Methods for accurate characterization of the modal frequencies of the system should be explored. In doing so better agreement between both uncoupled and coupled natural frequencies of the system can be attained.

- The effect of airfoil thickness and wall interference on the unsteady aerodynamic component must be accounted for. This can be done by careful consideration of Yate's Modified Strip Theory or other adequate theories in conjunction with computational fluid dynamics aerodynamic models.

- An investigation of the effect of tunnel turbulence on the dynamic response of the experimental system should be conducted. The first step is to install a flow quality sensor in the tunnel capable of measuring speed distributions and fluctuation level. CFD models will aid in achieving quantitative and qualitative results.

- Once confidence is established in the current simulations in predicting system behavior with freeplay, they can be used to determine the effect of nonlinear damping based on mathematical models already created at the University of Washington. An attainable and novel goal is to incorporate both nonlinearities simultaneously and analyzing their combined effect on system behavior.

BIBLIOGRAPHY

[1] M.D. Conner, D.M. Tang, E.H. Dowell, and L.N. Virgin. Accurate numerical integration of state-space models for aeroelastic systems with free play. *AIAA Journal*, 34(10):2202–2205, October 1996.

[2] M.D. Conner, D.M. Tang, E.H. Dowell, and L.N. Virgin. Nonlinear behavior of a typical airfoil section with control surface freeplay: A numerical and experimental study. *Journal of Fluids and Structures*, 11(1):89–109, January 1997.

[3] D. Tang, E.H. Dowell, and L.N. Virgin. Limit cycle behavior of and airfoil with a control surface. *Journal of Fluids and Structures*, 12:839–858, July 1998.

[4] J.T. Gordon. Nonlinear damping effects on control surface futter of a typical section airfoil. *International Forum on Aeroelasticity and Structural Dynamics*, June 2009.

[5] J.T. Gordon, E.E. Meyer, and R.L. Minogue. Nonlinear stability analysis of control surface futter with freeplay effects. *Journal of Aircraft*, 45(6):1904–1916, December 2008.

[6] E.H. Dowell, J. Edwards, and T. Strganac. Nonlinear aeroelasticity. *Journal of Aircraft*, Vol. 40(DOI: 10.2514/1.134), 2003.

[7] Theodore Theodorsen. General theory of aerodynamic instability and the mechanism of flutter. *NACA Report*, (No. 495), 1935.

[8] Matthew Nobel. *Nonlinear Aeroelastic Behavior of Tail/Rudder Systems with Freeplay and Actuator Failure.* MSAA thesis, University of Washington, 2013.

[9] Robert H. Scanlan and Robert Rosenbaum. *Introduction to the Study of Aircraft Vibration and Flutter*. The Macmillan Company, 1968.

[10] Francesca Paltera. *Flutter Response to Damage of Composite Aircraft Control Surfaces*. MSME thesis, University of Washington, Mechanical Engineering Department, 2008.

[11] J.R. Wright. *Introduction to Aircraft AerAeroelastic and Loads*, pages 412–415. John Wiley, 2007.

[12] Karthikeyan Duraisamy, William J. McCroskey, and James D Baeder. Analysis of wind tunnel wall interference effects on subsonic unsteady airfoil flows. *Journal of Aircraft*, 44(5), Sep-Oct 2007.

[13] E. Carson Yates. Modified-strip-analysis method for prediction wing flutter at subsonic to hypersonic speeds. *Journal of Aircraft*, 3(1), Jan-Feb 1966.

[14] A. Gelb and W.E. Vander Velde. *Multiple-Input Describing Functions and Nonlinear System Design*. McGraw-Hill, 1968.

[15] Steven H. Strogatz. *Nonlinear Dynamics and Chaos*. Perseus Books Publishing, LLC, 1994.

Appendix A

AERODYNAMIC FORCES AND MOMENTS AND THEODORSEN CONSTANTS

Total forces and moments on the aeroelastic system as a function of the Theodorsen constants defined below.

$$P = -\rho b^2 \left(v\pi\dot{\alpha} + \pi\ddot{h} - \pi ba\ddot{\alpha} - vT_4\dot{\beta} - T_1 b\ddot{\beta} \right) - 2\pi\rho vbC(k) \left[v\alpha + \dot{h} + b\left(\frac{1}{2} - a\right)\dot{\alpha} + \frac{1}{\pi}T_{10}v\beta + \frac{b}{2\pi}T_{11}\dot{\beta} \right] \quad \text{(A.1)}$$

$$M_\alpha = -\rho b^2 \left\{ \pi\left(\frac{1}{2} - a\right) vb\dot{\alpha} + \pi b^2 \left(\frac{1}{8} + a^2\right)\ddot{\alpha} + (T_4 + T_{10})v^2\beta + \left(T_1 - T_8 - (c-a)T_4 + \frac{1}{2}T_{11}\right) vb\dot{\beta} - [T_7 + (c-a)T_1]b^2\ddot{\beta} - a\pi b\dot{h} \right\} + 2\rho vb^2\pi\left(a + \frac{1}{2}\right) C(k) \left[v\alpha + \dot{h} + b\left(\frac{1}{2} - \alpha\right)\dot{\alpha} + \frac{1}{\pi}T_{10}v\beta + \frac{b}{2\pi}T_{11}\dot{\beta} \right] \quad \text{(A.2)}$$

$$M_\beta = -\rho b^2 \left\{ \left[-2T_9 - T_1 + T_4\left(a - \frac{1}{2}\right) \right] vb\dot{\alpha} + 2T_{13}b^2\ddot{\alpha} + \frac{1}{\pi}v^2\beta(T_5 - T_4T_{10}) - \frac{1}{2\pi}vb\dot{\beta}T_4T_1 1 - \frac{1}{\pi}T_3b^2\ddot{\beta} - T_1 b\ddot{h} \right\} - \rho vb^2T_{12}C(k) \left[v\alpha + \dot{h} + b\left(\frac{1}{2} - a\right)\dot{\alpha} + \frac{1}{\pi}T_{10}v\beta + \frac{b}{2\pi}T_{11}\dot{\beta} \right] \quad \text{(A.3)}$$

The Theodorsen constants as functions of non-dimensional hinge location, c, and non-dimensional elastic axis location, a, [7][9].

$$T_1 = -\tfrac{1}{3}\sqrt{1-c^2}(2+c^2) + c\cos^{-1}(c)$$
$$T_2 = c(1-c^2) - \sqrt{1-c^2}(1+c^2)\cos^{-1}(c) + c(\cos -1(c))^2$$
$$T_3 = -\left(\tfrac{1}{8}+c^2\right)(\cos^{-1}(c))^2 + \tfrac{1}{4}c\sqrt{1-c^2}\cos^{-1}(c)(7+2c^2) - \tfrac{1}{8}(1-c^2)(5c^2+4)$$
$$T_4 = \cos^{-1}(c) + c\sqrt{1-c^2}$$
$$T_5 = -(1-c^2) - (\cos^{-1}(c))^2 + 2c\sqrt{1-c^2}\cos^{-1}(c)$$
$$T_6 = T_2$$
$$T_7 = -\left(\tfrac{1}{8}+c^2\right)\cos^{-1}(c) + \tfrac{1}{8}c\sqrt{1-c^2}(7+2c^2)$$
$$T_8 = -\tfrac{1}{3}\sqrt{1-c^2}(2c^2+1) + c\cos^{-1}(c)$$
$$T_9 = \tfrac{1}{2}\left[\tfrac{1}{3}\left(\sqrt{1-c^2}\right)^3 + aT_4\right]$$
$$T_{10} = \sqrt{1-c^2} + \cos^{-1}(c)$$
$$T_{11} = \cos^{-1}(c)(1-2c) + \sqrt{1-c^2}(2-c)$$
$$T_{12} = \sqrt{1-c^2}(2+c) - \cos^{-1}(c)(2c+1)$$
$$T_{13} = \tfrac{1}{2}\left[-T_7 - (c-a)T_1\right]$$
$$T_{14} = \tfrac{1}{16} + \tfrac{1}{2}ac$$